Ignition of quantum cascade lasers in a state of oscillating electric field domains

David O. Winge,[1,2] Emmanuel Dupont,[3] and Andreas Wacker[1,*]

[1]*Mathematical Physics and NanoLund, Lund University, Box 118, 22100 Lund, Sweden*
[2]*Department of Physics, University of California San Diego, La Jolla, California 92093-0319, USA*
[3]*Advanced Electronics and Photonics Research Centre, National Research Council, Ottawa, Ontario K1A 0R6, Canada*

Quantum cascade lasers (QCLs) are generally designed to avoid negative differential conductivity (NDC) in the vicinity of the operation point in order to prevent instabilities. We demonstrate that the threshold condition is possible under an inhomogeneous distribution of the electric field (domains) and leads to lasing at an operation point with a voltage bias normally attributed to the NDC region. For our example, a terahertz QCL operating up to the current maximum temperature of 199 K, the theoretical findings agree well with the experimental observations. In particular, we experimentally observe self-sustained oscillations with GHz frequency before and after threshold. These are attributed to traveling domains by our simulations. Overcoming the design paradigm to avoid NDC may allow for the further optimization of QCLs with less dissipation from stabilizing background currents.

I. INTRODUCTION

The core of any laser is a gain medium, which is pumped strong enough that the gain overcomes the losses at threshold and the strong lasing field ignites. Typically, the medium is in a stationary state before threshold (while more complicated behavior such as relaxation oscillations may occur afterward). For electrically pumped lasers, this implies electric stability, which includes the avoidance of negative differential conductivity (NDC). This is a long-standing issue for the application of dispersive gain (also called Bloch gain) in semiconductor superlattice (SLs), where the gain mechanism is intrinsically related to NDC [1,2]. In this context, it was pointed out by Kroemer that once lasing is established, a stable operation point is possible in SLs, as the lasing field changes the electric behavior substantially [3]. In a region of NDC, a homogeneous electric field distribution in the transport direction is unstable and decays into regions with different electric fields, called field domains, as originally studied for Gunn diodes [4]. For SLs, domain formation [5–7] hindered the observation of dispersive gain [8,9] for a long time and no laser action has been realized so far. Thus, avoiding NDC is a common design paradigm of the related, technologically extremely successful quantum cascade laser (QCL) [10,11], as already pointed out in the precursory work [12]. While NDC and the formation of stationary domains have been observed and analyzed in some QCL structures [13–16], they are commonly considered to impede the desired lasing action.

In this work, we demonstrate that the operation of a QCL is also possible in the range of NDC, where the lasing field stabilizes the operation point similar to the never realized idea for SLs [3]. The key issue is the ignition of the lasing field, which occurs in a state of oscillating field domains, as shown both experimentally and by simulations. Our findings reveal an alternative type of laser ignition with interesting nonlinear behavior. Furthermore, lifting the paradigm of NDC in QCLs may also allow for new designs with higher performances.

Specifically, we consider a terahertz QCL structure, labeled V812, which was already studied in Ref. [17]. It shows lasing up to 199.3 K (with Cu waveguides), comparable to the current record of 199.5 K [18] for a similar device with higher current density. V812 belongs to the family of three-well designs with resonant tunnel injection and resonant phonon extraction [19]; see the band diagram at the nominal operation point (NOP) in Fig. 1(c). This class of designs has been previously shown to exhibit bias instabilities around threshold [17], when operated via a serial resistance. This is due to NDC occurring for biases after alignment of the injector level with the lower laser and extractor level, as common for tunneling in semiconductor heterostructures [5,12,20].

Figure 1(a) shows the generally sought scenario where the QCL ignites in a region without NDC; this example is a highly performant bound-to-continuum four-well structure [21]. After threshold, the lasing field causes stimulated emission, which enhances the current (dashed line) compared to the current without lasing (solid line). These data are obtained from our nonequilibrium Green's function (NEGF) model [22,23], where we assume a homogeneous bias drop along the structure allowing for periodic boundary conditions between the modules. For the device V812, studied here, we instead find a current peak at a bias of ~39 mV per module, which is below the NOP; see Fig. 1(b). Above this point, the current drops with bias, resulting in a region of NDC, which even covers the NOP at 54 mV per module, where the injector level aligns with the upper laser level. Thus, without stimulated emission, the NOP is not directly accessible. However, the current starts to increase at a higher bias, exhibiting a peak at 65 mV, where the upper laser level aligns with a further level 5.[1] We will

---

*Corresponding author: andreas.wacker@fysik.lu.se

---

[1]For its most part, level 5 corresponds to the second excited state of the lasing double well.
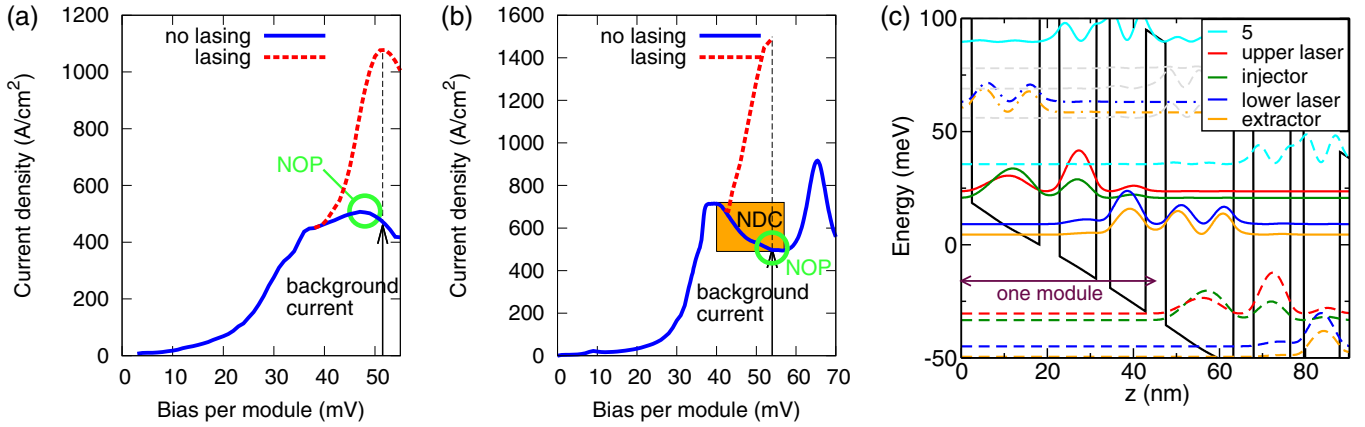
FIG. 1. Operating in the NDC region enhances the ratio between the lasing driven current and the background current: (a) Calculated current versus bias assuming a homogeneous field distribution for the sample [21]. The green circle depicts the nominal operation point (NOP). (b) Corresponding result for the sample V812 [17], which is considered here. (c) Conduction band profile and relevant electronic states (sequence between 0 and 50 meV as in legend and periodically shifted with different linestyles) at the NOP of 54 mV/module for the sample V812 where two modules are displayed. Starting from the extraction barrier, the layer sequence of a module is **46**/158/**46**/86/**31.7**/83 Å where the boldface font stands for $Al_{0.15}Ga_{0.85}As$ barriers and roman font indicates the GaAs wells. The center 5 nm of the 158 Å injector well is Si doped at $6 \times 10^{16}/cm^3$. The entire device contains 222 modules.

demonstrate how this tunnel resonance plays an essential role during laser ignition as it provides an operation point with positive differential conductivity exhibiting sufficient optical gain. For the self-consistent lasing field [red dashed line in Fig. 1(b)], where gain and losses compensate, the current is strongly increased, resulting in positive differential conductivity and stable operation around the NOP. This situation is in complete analogy with the scenario proposed for SLs [3]. Comparing Figs. 1(a) and 1(b), we find that the ratio between the lasing-induced current and the background current is actually higher for the QCL operating in the NDC region. For the bound-to-continuum structure in Fig. 1(a), further current paths through other levels prevent NDC. This results in a parasitic background current density at the operation point which acts as a source of dissipation [24]. For good diagonal designs such as the structure V812,[2] the current without lasing is actually low at the NOP, as a long lifetime of the upper laser state is envisaged. Thus, the scenario observed in Fig. 1(b) is actually beneficial, provided the ignition of the lasing field is guaranteed.

In this paper, we show how the ignition occurs in V812 by a detailed experimental and theoretical study. For this purpose, we extend the standard simulation schemes for domain formation for superlattices [6,7] and QCLs [14] by the interplay with the cavity fields, as taken into account by our microscopic NEGF simulations; see Appendix A 2. Using this model, we are able to simulate the ignition of the lasing field in the NDC region. The current-bias relation exhibits a "merlon" at threshold, in good agreement with the experimental data as discussed in Sec. II. Studying the time dependence of the

experimental bias, we observe self-sustained oscillations on the GHz scale both before and after threshold; see Sec. III. Within our model, these oscillations are attributed to traveling field domains. Furthermore, we validate the ignition scenario by the red shift of the lasing spectrum close to threshold in Sec. IV. Details on the simulations and experiments are given in Appendixes A and B, respectively. Appendixes C and D provide additional data from simulations and experiments with a different device. Finally, Appendix E addresses the distortion of the oscillation signal by the incomplete radio frequency (RF) design. Our findings clearly demonstrate the ignition scenario in the NDC region, which results in conventional lasing at the NOP, where the lasing-induced current stabilizes the operation.

II. FORMATION OF FIELD DOMAINS

Figure 2 shows an unusual scenario around ignition in the light (L), voltage (U_{QCL}), and current density (J) characteristics, where the voltage has a flat local maximum (referred to as merlon) around 700 A/cm², as highlighted by the colored areas in Fig. 2(b). Simultaneously, the light intensity exhibits a peak, while at higher current density ($\gtrsim$800 A/cm²) a common linear increase of intensity and bias is observed. The results from our model with domain formation, see Fig. 2(c), agree reasonably well with the experimental observation in Fig. 2(b).

The global scenario leading to the merlon is shown in Fig. 2(a). The $U_{QCL} - J$ relation is obtained by operating via a load resistance and a parallel capacitance with an external bias U_0, the output voltage from the pulser. (The circuit model is further discussed in Appendix A 2.) If the load line is shifted to the right of the first current peak around 39 mV per module, a domain state is established in the QCL, which results in the red solid horizontal line, also called current plateau. Here the total bias is distributed on a low- and a high-field domain [shown in greater detail in Fig. 4(a)]. The high-field domain exhibits gain (at a frequency slightly higher than the NOP), and the total gain, as expressed by Eq. (A7), gets close to the losses if the

---

[2] The "diagonality" of a design is related to spatial separation between lasing states and is commonly assessed by the oscillator strength, here 0.3 in the V812 structure. As the oscillator strength between lasing states is lower, the laser design becomes more diagonal.
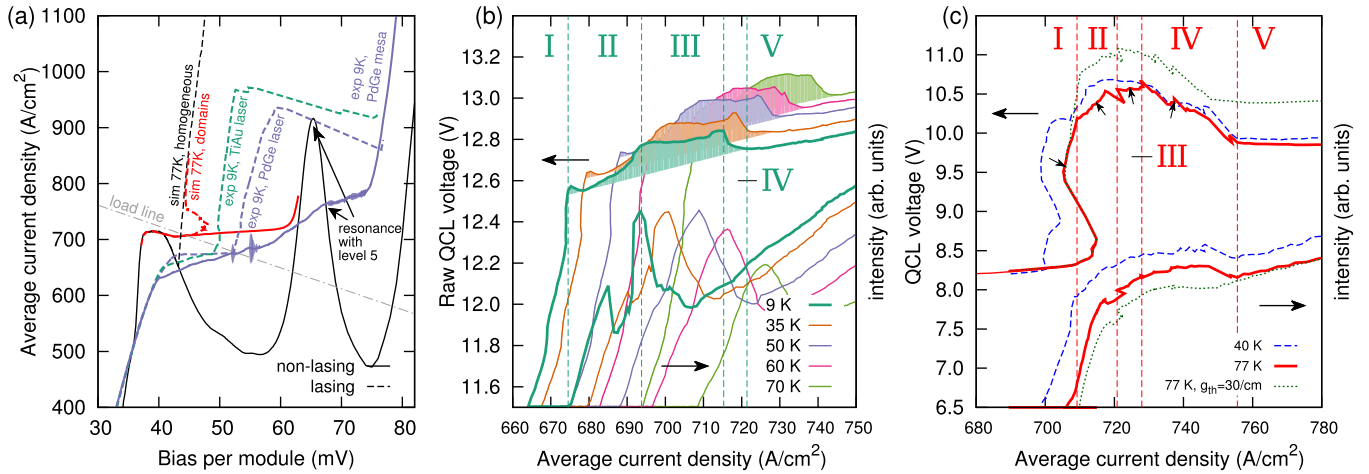
FIG. 2. Current-voltage relations with domain formation: (a) Quantitative comparison of experimental and simulated current-voltage characteristics. Data taken at 9 K from three devices fabricated with different contacts and waveguide sizes are shown. (See Appendix B for the derivation of experimental bias per module.) The three thicker sections in the electrical characteristic of the PdGe mesa (purple solid) are proportional to the amplitude of voltage self-oscillations, or instabilities, as measured with 1-GHz bandwidth oscilloscope. The theoretical domain solution (red line) without (solid) and with (dashed) the lasing field is compared to the corresponding result for a homogeneous bias drop, as shown by the black line. The dash-dotted dark gray line denotes the load line in Eq. (A3). (b) Zoom in on the experimental current-bias relation and lasing intensity around threshold for different temperatures for the TiAu laser. The signification of "raw" QCL voltage, the vertical axis label, is explained in Appendix B. (The temperatures are ordered from 9 K (left) to 70 K (right) at the bottom of the figure.) (c) Simulated results comparing the effects of temperature and total losses. In panel (a) and elsewhere in the paper, losses of 20 cm^{-1} and a temperature of 77 K are applied to the simulations. The vertical dashed lines in panels (b) and (c) indicate the boundaries between the regions I–V at 9 and 77 K, respectively. The small arrows in panel (c) mark the operation points shown in Fig. 4.

high-field domain becomes large enough. The onset of lasing changes the local current-field relation, which gives rise to the pronounced merlon of the dashed red line. For even higher currents, this domain state merges with the homogeneous state under lasing (black dashed line), demonstrating that the conventional lasing around the NOP is stabilized due to the lasing-induced current.

The merlon feature occurs for a wide range of temperatures up to 90 K in our sample; see Fig. 2(b). Both in experiment and simulation, it is shifted to higher currents with increasing temperature; see Figs. 2(b) and 2(c). In Fig. 2(c), we also show simulations for an increased threshold gain g_{th}, which shifts the bias but does not change the essential feature. Such a shift also occurs between devices with different metallization of the electric contact; see Fig. 2(a). A similar merlon is also observed between 89 and 105 K for the structure V773 of Ref. [17].

Around the merlon, we identify five regions, as indicated in Figs. 2(b) and 2(c). In region I, U_{QCL} increases with relatively little variation of current, as is common for domain formation, where the increase in bias corresponds to a spatial increase of the high-field domain. At the experimental threshold, we observe a kink in U_{QCL} [together with a small spike (∼20 mV) in Fig. 2(b) at low temperature]. Subsequently, a joint increase of current and bias marks region II, the left flank of the merlon. Both in experiment and simulation, the lasing intensity is drastically increasing in this region. This is followed by region III, the top of the merlon, where the bias is almost constant and the calculated lasing intensity shows less variation, while a drop is observed in the experiment. The latter may be partially related to the drop in laser frequency occurring here (see Sec. IV) and associated changes in mirror losses. On the right flank of the merlon, region IV, the bias drops with current.

Finally, in region V, the bias and intensity increase almost linearly with current as common for lasing operation within a homogeneous field distribution.

Figure 2(a) also provides a comparison between the experimental $U_{QCL} − J$ characteristics of three devices, processed with either TiAu or PdGe contacts. The PdGe mesa device was purposely fabricated to frustrate stimulated emission. The $U_{QCL} − J$ of this device (purple solid line) shows two pronounced shoulders at average biases of 40 and 68 mV per module, without any detailed structure in between. This confirms our simulation data (black solid line), which show current peaks close to these biases, but, without lasing, no current peak at the operation point of 54 mV per module. Voltage fluctuations, as recorded with a 1-GHz bandwidth oscilloscope, are overlaid on the current density of the PdGe mesa device in Fig. 2(a). They can be regarded as a sign for NDC both between the shoulders and after the shoulder at ∼68 mV/module. Laser emission on the low-loss waveguide, i.e., with TiAu contacts, collapses after 55 mV/module, close to the predicted NOP, a voltage corresponding to the optimum injection to the upper laser state, which is now accessible thanks to stimulated emission. This is in contrast with the higher loss waveguide device, i.e., with PdGe contacts, where laser emission switches off later, above 60 mV/module.

The simulated increase of current above 75 mV per module is due to tunneling from the lower lasing level to level 5 (aligned at ∼83 mV per module) and subsequent leakage to continuum. As the current in the continuum is not well covered in our model, the simulations underestimate the current here. Overall, the simulated current densities and biases agree well with the experimental data.
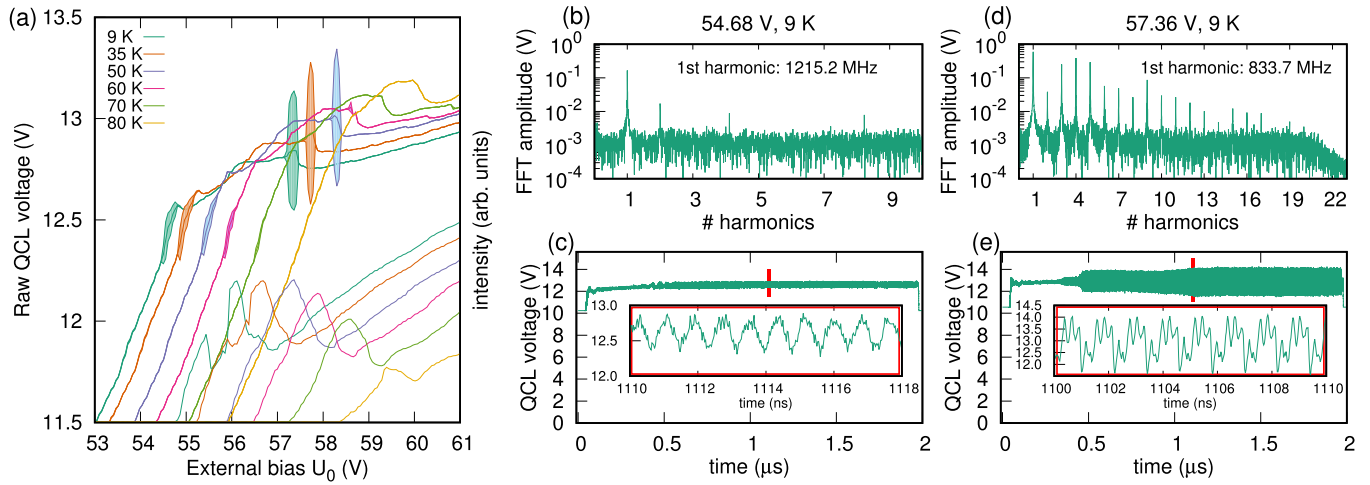
FIG. 3. Oscillatory behavior detected experimentally: Panel (a) shows the same data as presented in Fig. 2(b) but plotted against external bias U_0. (The temperatures are ordered from 9 K (left) to 80 K (right) at the bottom of the figure.) The shaded regions indicate voltage oscillations monitored by an oscilloscope with 1-GHz bandwidth, which are observed in two different ranges of bias for temperatures below 70 K. For 9 K, we show the QCL voltage, as measured with a 15-GHz bandwidth real-time oscilloscope, during the 2-μs pulse at $U_0 = 54.68$ V and 57.36 V in panels (b)–(e), respectively, which are representative for the two different regions of oscillation. The amplitude spectrum shown in panels (b) and (d) are taken for the time interval $1.08\,\mu s \leqslant t \leqslant 1.28\,\mu s$ of the pulses displayed in panels (c) and (e). In panel (d), up to 20 harmonics can be observed, hence demonstrating that the sharp and small features in the time-resolved voltage in panel (e) are highly periodic. Because of the incomplete RF design, details of the oscillations on the subnanosecond timescale in panels (c) and (e) may be improperly recorded; see Appendixes E and B.

III. OSCILLATING FIELD DOMAINS

Figure 3 shows self-sustained bias oscillations measured experimentally. As exemplified in Figs. 3(c) and 3(e), they occur both below and above threshold. The shaded regions in Fig. 3(a) show the extend of the oscillatory behavior as monitored with the 1-GHz bandwidth oscilloscope; see Appendix B. With a high-bandwidth real-time oscilloscope, we observe GHz oscillations up to a temperature of 78 K in parts of region III and the transition to IV. Here, we measure frequencies in the range of 0.8–0.9 GHz, which are decreasing with bias for each temperature. In region I, the less intense GHz oscillations are detected up to 68 K. The frequencies are around 1.2 GHz and increase up to slightly 1.3 GHz above threshold. The laser ignites while the voltage self-oscillates; nevertheless these oscillations are quickly damped as the bias increases above threshold (beginning of region II); see also Fig. 14 in Appendix D for the oscillations around threshold. The measurement of the bias dependence of the oscillation frequency is described in Appendix D.

The occurrence of oscillations with GHz frequency can be understood on the basis of traveling field domains as known from Gunn diodes [4] and superlattices [6,7]. For the low doping density, the NDC region cannot be overcome by charge accumulation in a single module [6,25]. Based on the current and electron density, we estimate an average drift velocity of 6.6 km/s, with which these excess carriers between the domains travel through the structure. As a new accumulation layer forms only after the preceding one has traversed a large part of the device with a length of 10 μm, we get a typical oscillation period of 1 ns.

Such oscillations based on traveling field domains are found in our simulations as shown in Fig. 4 for a selected set of operation points in the current-bias relation (extensive

data can be found in Appendix C). Here we find different oscillation modes in the different regions of the current-bias characteristics, labeled I–IV in Fig. 4. The reason is that the local current-field relation is strongly modified by the lasing field.

In region I, the lasing field does not play a role and the local current-field relation [as given by the black line in Fig. 1(b)] is unaltered. Within the domains, the condition of a constant current density implies the bias drop per module of ≈ 38 and ≈ 62 mV, in the low- and high-field domains, respectively. Between both domains, there is a layer of electron accumulation [e.g., around module 150 at 6 ns in Fig. 4(a)], which travels toward the positive contact. From time-resolved electron density plots, we find that the accumulation layer spans over several modules ($\sim 3-6$). The movement of the accumulation front provides a drop in bias and, following the load line, an increase in current. Eventually, the current reaches the first peak in the local current-field relation, where the low-field domain becomes unstable and a new domain boundary forms (e.g., around module 130 at 8 ns). These oscillations exhibit frequencies of 0.4–0.6 GHz [as can be seen in Figs. 10 and 11 of Appendix C], increasing with external bias U_0 in accordance with measurements.

In region II, the lasing field is strong enough to alter the local current relations, resulting in the surge for the average current; see Fig. 2. Lasing sets in just after the forming of the high-field domain [e.g., at 12 ns in Fig. 4(b)]. The increased current results in a drop of field in the high-field domain, as conduction plus displacement current has to match the current in the low-field domain. In the following, the accumulation front travels, reducing the extend of the high-field domain and the total gain drops, so that lasing operation stops. While the accumulation front travels further, the low-field domain
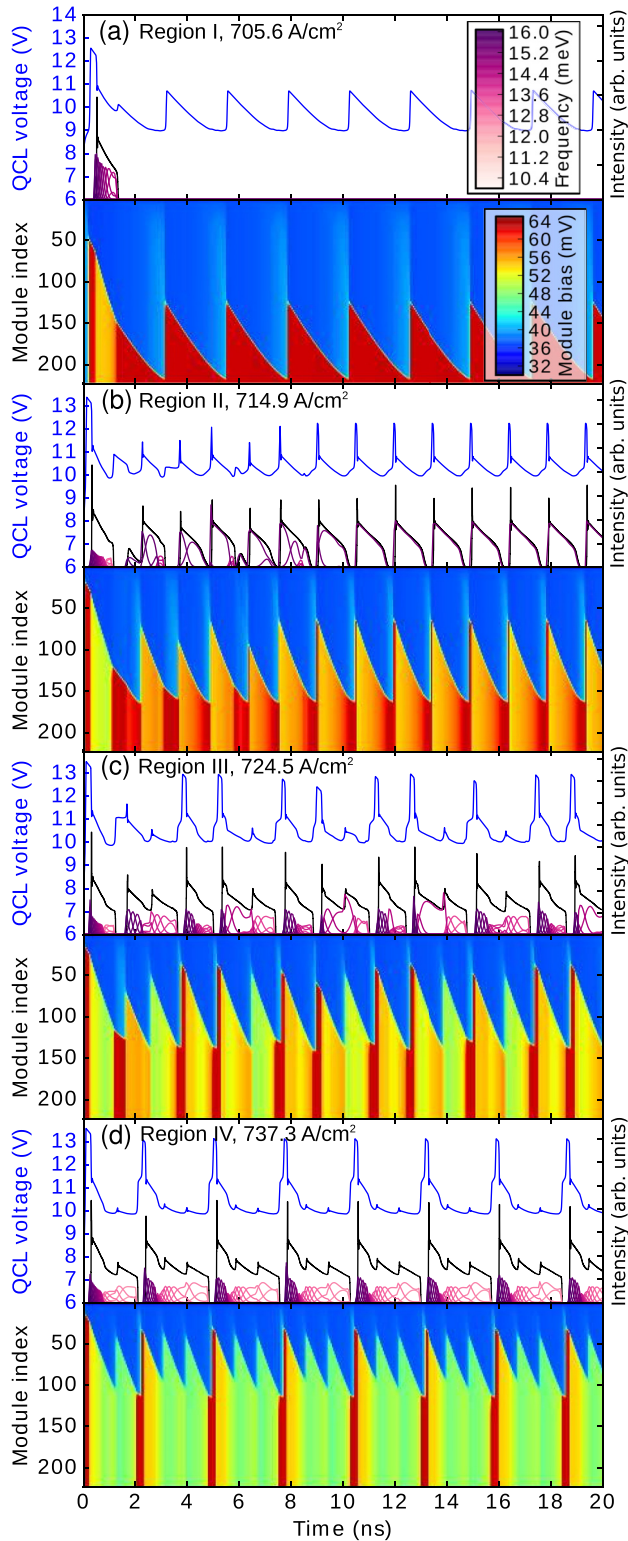
FIG. 4. Simulated oscillations for four different operation points as indicated in Fig. 2(c). For each panel, the space and time dependence of the electric field is displayed in color scale. The bottom module ($m = 222$) is next to the positive contact. The upper part of each panel shows the bias along the QCL structure (blue) and the total lasing intensity (black), which is also resolved for the individual modes with frequency marked by color. Data for further operation points and Fourier transforms of the voltage signals are displayed in Appendix C.

reaches the first current peak and a new domain boundary forms similar to region I.

Upon increasing the external bias to region III, the new instability may occur, while lasing is still active. Then the new high-field domain arises at a lower field around 50 mV per module [e.g., at 10 ns in Fig. 4(c)]. However, starting from this state, lasing always stops before the next domain forms and we observe an irregular (possibly chaotic, but we did not prove this) pattern in Fig. 4(c) or different types of locking between both scenarios; see Fig. 12 in Appendix C.

In region IV, see Fig. 4(d), lasing prevails most of the time and at least half of the high-field domains are formed close to the NOP with fields around 50 mV per module. This provides the drop in average bias as characteristic for this region. While new domains form about once per ns, the fundamental oscillation frequency is 0.37 GHz in Fig. 4(d) as only every third time the lasing operation stops.

Comparing with the experimental oscillations, the shape of the bias signal in region I is triangular both in experiment, Fig. 3(c), and simulations, Fig. 4(a). The bias signal in regions III and IV resembles more a switching between plateaus with bias values separated by 1 V. Here the experimental data, Fig. 3(e), do not show the thin bias spikes visible in Figs. 4(c) and 4(d). Instead, a strong ringing-like feature with a pseudoperiod of 0.2–0.3 ns is observed, which is attributed to lacking RF design (see Appendix B). An attempt to filter out ringing effects has been tested and some deconvolution results are reported in Appendix E. The simulated frequency of the oscillations in region I ($\sim$0.5 GHz) is lower than the experimental results ($\sim$1.2 GHz), while in region III the experimental frequency well matches the mean rate of domain formations (both $\sim$0.8 GHz). In region III, we also detected a subharmonic regime at a specific bias range, see Fig. 16 in Appendix D and Fig. 17(b) in Appendix E, which might indicate different coexisting domain ignition processes as observed in the simulations in regions III and IV. The main discrepancy is that the simulations provide oscillations throughout all the regions I–IV, while experimentally they are only clearly detected within parts of the regions I, III, and IV (the latter is small in the experiment), as shown in Fig. 3(a). However, we experimentally observed strongly enhanced noise on voltage, light intensity, and phase on the lock-in amplifier used during THz detection in regions II and III, which we could not fully explain yet. In this context, we note that the stability of domains depends on the details of the electron distribution in the transition region between the domains, the nature of the injecting contact, and the external circuit (for instance, the 50 Ω coaxial cable was not considered in simulations). For these issues, we did rather simple approximations, which are difficult to overcome as no consistent treatment has been proven valid so far. Furthermore, pinning of the accumulation layer may occur if individual modules differ due to growth imperfections. These effects could also cause the differences between the measured and simulated oscillation frequencies.

IV. LASING SPECTRA

For the ignition scenario from a domain state discussed here, the high-field domain exhibits a higher bias drop per module than the final lasing state. Because of the Stark shift,
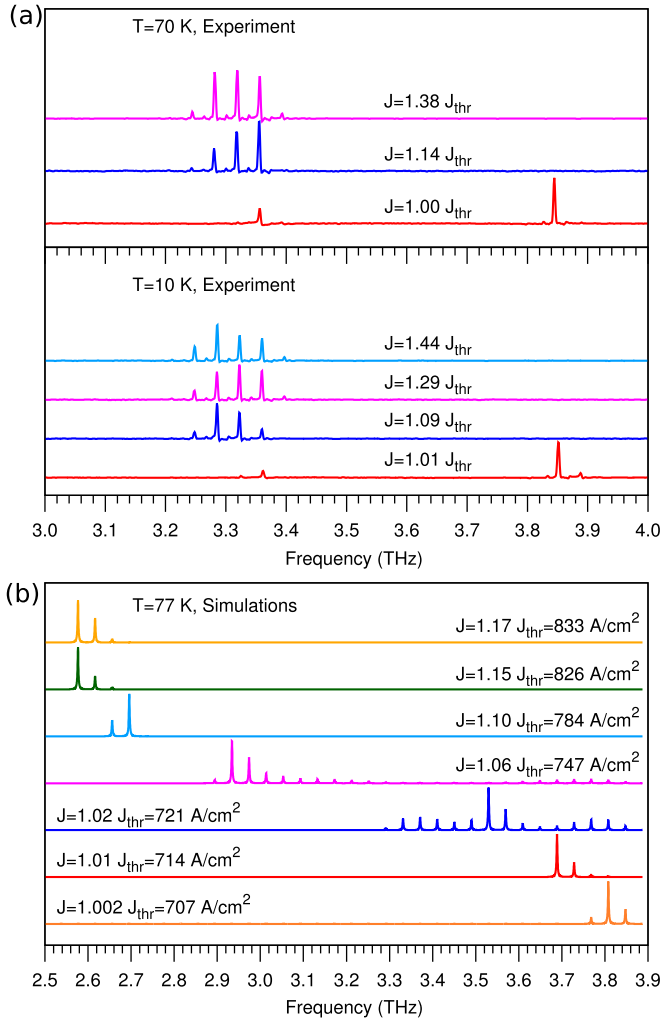
FIG. 5. Lasing spectra demonstrating a significant red-shift after threshold: (a) Experimental spectra for the sample V812 at different temperatures and currents. Close to threshold, a high-frequency signal can be seen at 3.84 THz, while lower frequencies around 3.3 THz are observed for higher current. (b) Simulated spectra at different current densities plotted with a linewidth of 0.2 GHz. Lasing starts in a high-field domain, see, e.g., Fig. 4(b), and is shifted toward the lower frequencies as current increases.

which is substantial for a diagonal design as V812, we thus expect a higher lasing frequency at ignition. Figure 5 shows that this is indeed the case. Just after threshold, the lasing frequency is around 3.8 THz in the experiment and slightly lower in the simulation. With increasing current a drop to 3.3 THz (experiment) or 2.6 THz (simulations) is observed, where the frequencies remain constant with further increase of current. The discrepancy in frequency for operation in region V is related to the lower threshold bias in the simulations. Figure 2(a) shows that the lasing around 800 A/cm² occurs at 45 mV per module in the simulations and at 50 mV per module in the experiment. Thus, the difference in frequency corresponds to the Stark shift. E.g., for an operating bias of 52 mV per module, the simulations show a gain peak at 3.1 THz (see also Fig. 8 in Appendix A 3), in much better agreement with the experimentally observed lasing. A similar spectral red

shift after threshold was also observed in the more diagonal structure V773 of Ref. [17].

V. CONCLUSION AND OUTLOOK

The onset of lasing from a state of oscillating electric field domains was demonstrated for THz QCLs. Comparing experimental and theoretical results, this feature is clearly reflected in the shape of the current-bias relation, characteristic self-sustained oscillations around threshold, and the red shift in the optical spectra just after threshold.

This ignition type demonstrates that there is no need for positive differential conductivity for the NOP at threshold, which is also visible in other highly performing QCLs [17,26]. Instead, significant gain at a resonance at higher field is sufficient. In this case, domain formation in the NDC region allows a part of the device to operate at this auxiliary operation point. After ignition of the lasing field, the stimulated transitions provide sufficient current at the NOP to break the NDC. Thus a conventional requirement for laser design is lifted, which allows for more flexibility in the design of QCLs at the price of noiselike behavior at threshold. In particular, such a new design could reduce the background current and provide more effective power conversion to the lasing field. In order to realize this scenario, during the design stage of highly diagonal structures particular attention should be paid to the gain at the positive differential resistance region next above the NOP.

Furthermore, we found complex oscillation patterns due to the interplay between the lasing field and the running field domains. This establishes a further degree of freedom compared to the related superlattices with their rich spectra of nonlinear and chaotic behavior [27–29]. In this context, the time-resolved measurement of the lasing activity with a fast THz detector [30] could provide additional relevant data.

APPENDIX A: SIMULATION PROCEDURE

1. NEGF simulations for homogeneous field distributions

Our calculations are based on the NEGF model [22,23], providing us with the current density $J(F_{dc}, F_{ac}, \omega_0)$ and gain $G(F_{dc}, F_{ac}, \omega_0)$, which are nonlinear functions of the electric field $F(t) = F_{dc} + F_{ac} \cos(\omega_0 t)$. Here F_{dc} is the field due to an applied bias and F_{ac} is the electrical component of the lasing field in the waveguide with frequency ω_0. As is common for most simulation schemes [31], these calculations assume a homogeneous bias drop along the QCL structure. To calculate the current under operation, we increase the ac field strength at each bias point until gain is saturated by the level of the
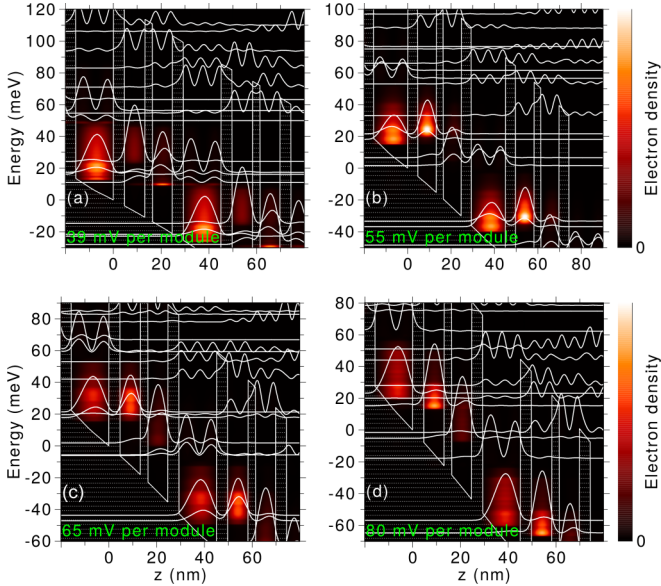
FIG. 6. Electron density calculated by the NEGF approach for different biases per module together with the Wannier-Stark levels.

losses g_{th}. In addition, the peak gain frequency is updated with the ac field strength to track intensity-dependent effects on the laser transition. This procedure provides the data presented in Figs. 1(a) and 1(b). The temperature used in the simulations defines the thermal occupations of the phonon modes. Because of the excitation of the mostly relevant optical phonons on short timescales [32,33], this temperature should be higher than the experimental heat sink temperature. As input, we use the nominal sample parameters together with an exponential interface roughness model [34] with 0.2 nm height and 10 nm lateral correlation length. All these model details agree with Ref. [23], where results for a large number of devices are shown. Note that we define the bias U_{QCL}, electric field F, and electric current (density) $I(J)$ with an additional minus sign throughout the paper to compensate for the negative electron charge $-e$.

In Fig. 6, we show the calculated electron densities together with the Wannier-Stark levels for different biases, in order to study the relevant alignments. For a bias of 39 mV per module [Fig. 6(a)], the injector states aligns with the lower laser level and the extractor state, allowing for a strong current through the entire module. This is just the first current peak in Fig. 1(b). The resonance at 65 mV is shown in Fig. 6(c) and the increasing current around 80 mV [see Fig. 2(a)] is attributed to tunneling to continuum states in Fig. 6(d). Here, we used nine states per module and next-nearest neighbors in the simulations. For biases below 70 mV per module, we found that seven states per module were sufficient, which allows us to reduce the numerical effort.

In order to simulate domain formation with the interplay of an intracavity lasing field, as shown in Fig. 2, the gain needs to be estimated at frequencies ω, which may differ from ω_0 of the lasing field. A common situation in this study is that lasing sets in in the high-field domain, allowing for a buildup in intensity at the frequency favored at that field strength. As intensity increases, the local current-field relation changes to
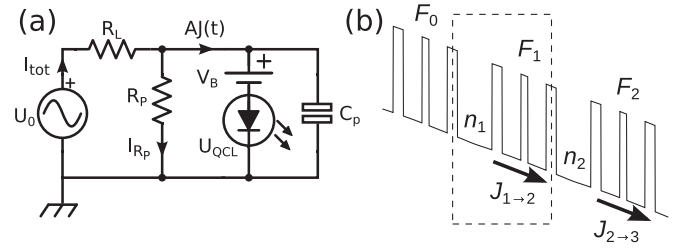

FIG. 7. (a) Circuit including a parasitic capacitance C_p in parallel to the QCL as well as a voltage probe of resistance R_p, a load resistance R_L, and a Schottky voltage barrier V_B as well as the pulser at an external bias of U_0. In addition to this model, a 50-Ω coaxial cable connects the pulsed bias source to the load which is neglected here. The voltage probe resistance R_p includes the 50-Ω input impedance of the oscilloscope. (b) Numbering of electron densities n_m, fields F_m, and current densities $J_{m\to m+1}$.

a degree, where lasing at other frequencies is more favorable compared to the original one. This poses the question: How does the established laser field promote the onset of lasing at other frequencies? To answer this, multidimensional fitting of the simulated NEGF data is not enough, as we need to estimate the gain at frequencies other than the lasing frequency. Our approach is to use fits for the current density $J^{\mathrm{fit}}(F_{\mathrm{dc}}, F_{\mathrm{ac}}, \omega_0)$ and gain $G^{\mathrm{fit}}(F_{\mathrm{dc}}, F_{\mathrm{ac}}, \omega_0, \omega)$ which are based on a simple physical model (see Appendix A 3) and where the parameters are determined by comparing with the full NEGF calculations.

2. Domain formation and external circuit

In this section, we describe the simulation of the extended QCL structure with $N = 222$ modules within the circuit shown in Fig. 7(a). In particular, we drop the assumption of a periodic voltage drop along the QCL structure, which lifts the requirement for charge neutrality in each module of the QCL. Instead, the electron density n_m in module m may differ from the background doping n_D (both in units 1/area). Here we assume that the additional charge of each module is essentially located in the injector well [the widest well of the structure; see Fig. 1(c)] and that the current density $J_{m\to m+1}$ between the injector wells m and $m + 1$ essentially depends on the bias drop $F_m d$ over module m. The numbering is illustrated in Fig. 7(b). Following Ref. [35], Ampere's law and Poisson's equation provide

$$\epsilon_r \epsilon_0 \frac{dF_m}{dt} = J(t) - J_{m\to m+1}$$

$$- \frac{C_p}{C_s + C_p}\left(J(t) - \frac{1}{N+1}\sum_{i=0}^{N} J_{i\to i+1}\right), \quad \text{(A1)}$$

$$n_m = n_D + \frac{\epsilon_r \epsilon_0}{e}(F_m - F_{m-1}), \quad \text{(A2)}$$

where $J(t)$ is the current density flowing into the QCL device and $C_s = A\epsilon_r\epsilon_0/d(N+1)$ is the intrinsic QCL capacitance assuming an average relative dielectric permittivity $\epsilon_r = 12.9$ for the active region with the cross section $A = 0.15\,\mathrm{mm}^2$ and a module thickness $d = 45.07\,\mathrm{nm}$. We use the parasitic capacitance $C_p = C_s/4$ and checked explicitly that larger values like $C_p = 4C_s$ hardly change the results. Operating via

a load resistor R_L, the circuit in Fig. 7(a) provides

$$AJ(t) = \frac{U_0}{R_L} - [U_{\text{QCL}}(t) + V_B]\left(\frac{1}{R_p} + \frac{1}{R_L}\right) \qquad \text{(A3)}$$

with

$$U_{\text{QCL}}(t) = \sum_{m=0}^{N} F_m(t)d, \qquad \text{(A4)}$$

where V_B is the Schottky barrier and R_p is the voltage probe resistance. Throughout the paper, we use $R_L = 41.2\,\Omega$, $R_p = 1050.4\,\Omega$, and $V_B = 0.8\,V$ in our simulations. The load curve of Eq. (A3) does not consider the effect of the residual resistance of the ground electrode on Si carrier, as addressed in Appendix B. Determining the current density $J_{m \to m+1}$ within a module is far from trivial, as we have to take into account a nonperiodic situation and carrier densities differing from the doping. Following the common approximation for superlattices [6,7] and QCLs [14], we use

$$J_{m \to m+1} = J^{\text{fit}}(F_m, F_{ac}, \omega_0)\frac{n_m - n_{m+1}e^{-eF_m d/k_B T}}{n_D - n_D e^{-eF_m d/k_B T}}. \quad \text{(A5)}$$

This expression is only defined for $1 \leqslant m < N$, as a real injector well is required on both sides. In order to close the equation system, we further need the cases $m = 0$ and $m = N$. Here we assume Ohmic boundary conditions

$$J_{0 \to 1} = \sigma_l F_0 \quad \text{and} \quad J_{N \to N+1} = \sigma_l F_N \frac{n_N}{n_D} \qquad \text{(A6)}$$

with the conductivity $\sigma_l = 0.15$ A/Vcm, which is chosen to be higher than the average conductivity in the QCL structure. This modeling follows essentially [14], where domain formation in QCLs was studied. Going beyond this work, we also consider the coupling to the lasing field here.

The waveguide modes constitute a global coupling between the modules. Each mode i is associated with a constant frequency ω_0^i, an electric field strength F_{ac}^i, and its average photon number $N_{\text{ph}}^i \propto (F_{ac}^i)^2$. Similarly, the gain in the waveguide is obtained by the average over all modules, where we assume that the gain is proportional to the electron density in the respective module:

$$\bar{G}(\omega, \{N_{\text{ph}}^i\}) = \frac{1}{N}\sum_{m=1}^{N}\frac{n_m}{n_D}G^{\text{fit}}(F_m, \{N_{\text{ph}}^i\}, \{\omega_0^i\}, \omega). \quad \text{(A7)}$$

Here the gain in each module is subject to saturation from all cavity modes. The gain recovery time is given by the timescales for scattering and tunneling in the modules, which are typically $\lesssim 1$ ps. This is shorter than the photon lifetime of 6 ps (for the gain threshold of $20\,\text{cm}^{-1}$), so that we can assume that the gain is an instantaneous function of the intensity. For the photon numbers, we thus have

$$\frac{dN_{\text{ph}}^i(t)}{dt} = \left[\bar{G}(\omega, \{N_{\text{ph}}^i\}) - g_{\text{th}}\right]\frac{c}{n_g}N_{\text{ph}}^i(t) + \sum_m \frac{An_m^{\text{ULS}}}{\tau_{\text{sp}}^i}$$

$$\text{(A8)}$$

for all cavity modes i, where $n_g = 3.6$ is the group refractive index (assumed to be constant here), and $g_{\text{th}} = 20\,\text{cm}^{-1}$ is given by the waveguide and mirror losses. A similar approach

to model the photon density in a THz QCL was reported in Ref. [36].

The last term in Eq. (A8) describes the spontaneous emission of light from electrons in the upper laser level into the lasing mode i, which is crucial for ignition. Assuming a plane wave in our metal-metal waveguide, we can use the standard textbook expression for the spontaneous emission rate (see, e.g., Eq. (8.3-6) of Ref. [37])

$$\frac{1}{\tau_{\text{sp}}^i} = \frac{\pi e^2 \omega_i}{\epsilon_r \epsilon_0 A L}|z_{lu}|^2 \mathcal{L}(\hbar\omega_i - E_u + E_l), \qquad \text{(A9)}$$

where z_{ul} is the matrix element between the upper and lower laser states, $L = 10\,\mu\text{m}$ is the thickness of the waveguide, and $\mathcal{L}$ is the Lorentzian from Eq. (A11) replacing the δ function. For different operation points, we find typical values $\tau_{\text{sp}}^i \approx 3\text{–}6$ ms. For simplicity, we choose $\tau_{\text{sp}}^i \approx 3$ ms for all simulations. This value is appropriate for the high-field domain with $eF_{\text{dc}}d \approx 62$ meV, where lasing typically sets in. (Here ω_i is large and Γ is small; see Fig. 8.) We checked explicitly that increasing τ_{sp}^i by a factor of 2 hardly changed the results.

3. Effective model of a single module

In order to fit the current and the gain, we use expressions resulting from a simple two-level model onto which the NEGF results are mapped. We consider an injecting current J_{inj} into level 2, scattering lifetimes τ_1, τ_2 for levels 1 and 2, respectively, and τ_{21} for scattering from 2 to 1. A laser field closely resonant to the energy difference E_{21} induces a transition rate, which, according to Fermi's golden rule [38], is proportional to the square of the oscillating field:

$$W_{2 \to 1} = \gamma_{12}(\omega)F_{\text{ac}}^2 \quad \text{with}$$

$$\gamma_{12}(\omega) = \frac{2\pi}{\hbar}\left|\frac{ez_{21}}{2}\right|^2 \mathcal{L}(E_{21} - \hbar\omega), \qquad \text{(A10)}$$

where the energy-conserving δ function is replaced with the more realistic Lorentzian

$$\mathcal{L}(E) = \frac{1}{2\pi}\frac{\Gamma}{E^2 + \Gamma^2/4}. \qquad \text{(A11)}$$

Under irradiation with ω_0 we can thus establish the rate equations, following Ref. [11],

$$\frac{dn_2}{dt} = \frac{J_{\text{inj}}}{e} - \frac{n_2}{\tau_2} - \gamma_{12}(\omega_0)F_{\text{ac}}^2(n_2 - n_1),$$

$$\frac{dn_1}{dt} = \frac{n_2}{\tau_{21}} - \frac{n_1 - n_1^{\text{th}}}{\tau_1} + \gamma_{12}(\omega_0)F_{\text{ac}}^2(n_2 - n_1),$$

where the second term of the equation for n_1 makes sure that the population reaches its thermal equilibrium value n_1^{th} in the absence of the injecting current and ac field. For the steady state, we obtain the inversion $\Delta n_{21} = n_2 - n_1$

$$\Delta n_{21} = \tau_2 \frac{\tau_{21} - \tau_1}{\tau_{21}}\frac{J_{\text{inj}}}{e} - n_1^{\text{th}}$$

$$- \left(\tau_1 + \tau_2\frac{\tau_{21} - \tau_1}{\tau_{21}}\right)\gamma_{12}(\omega_0)F_{\text{ac}}^2\Delta n_{21}, \quad \text{(A12)}$$
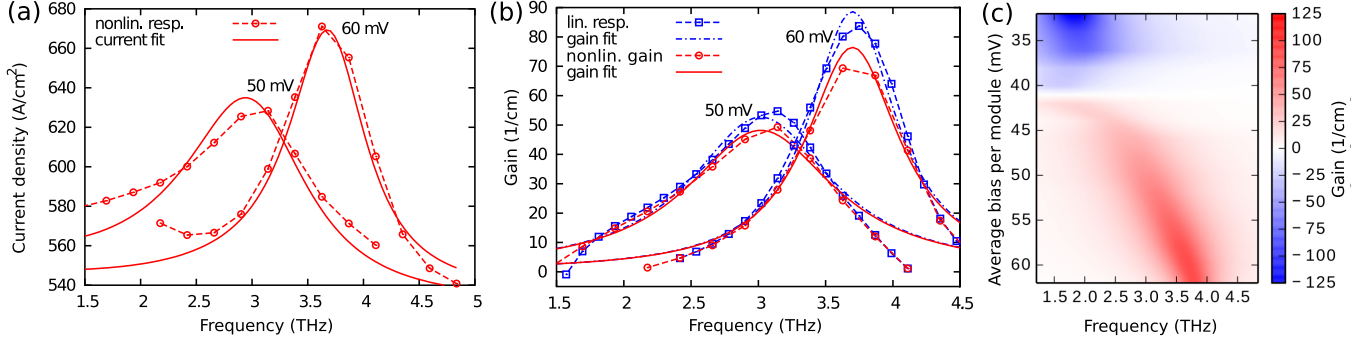
FIG. 8. In panels (a) and (b), we compare the NEGF results (shown as dashed lines with symbols) with the fitted effective expressions for current, Eq. (A17) [full lines in panel (a)], and gain, Eq. (A15) [dash-dotted lines for linear response, full lines for nonlinear response in panel (b)], respectively. The nonlinear response, i.e., simulations using a finite field strength of $eF_{ac}d = 5$ meV, is shown by dashed lines with circles, whereas linear response calculations, only panel (b), are shown with dashed lines with squares. Panel (c) shows a map of the gain as a function of frequency and bias per module as obtained from G^{fit} for low F_{ac}.

where right-hand side of the first line corresponds to the inversion Δn_{21}^0 for vanishing ac field strength. Thus,

$$\Delta n_{21} = \frac{\Delta n_{21}^0}{1 + \bar{\tau}\gamma(\omega_0)F_{ac}^2} \qquad (A13)$$

with $\bar{\tau} = \tau_1 + \tau_2(1 - \tau_1/\tau_{21}) \approx \tau_1 + \tau_2$ as the ratio τ_1/τ_{21} should be minimized for a good QCL design. Following Ref. [39], we can relate the linear response gain for a two-level system to the γ factor as

$$G_{12}(\omega) = \frac{2\hbar\omega}{c\epsilon_0\sqrt{\epsilon_r}d}\gamma_{12}(\omega)\Delta n_{21} . \qquad (A14)$$

Following Ref. [40], Eq. (A13) provides the gain saturation

$$G^{fit}(F_{dc}, F_{ac}, \omega_0, \omega) = \frac{G_{12}^0(\omega)}{1 + \bar{\tau}\gamma(\omega_0)F_{ac}^2} . \qquad (A15)$$

Here, $G_{12}^0(\omega)$ is the unsaturated linear response gain from Eq. (A14) with $\Delta n_{21} = \Delta n_{21}^0$. Note that we have now separated the pumping ac field at frequency ω_0 from the probe at ω, which means that we can now probe the saturated gain at a chosen frequency going beyond our NEGF simulations, where only a single frequency $\omega = \omega_0$ appears.

Under the assumption that the bottleneck for current is the inverted population at the laser transition, the total current will be a sum of stationary and induced current following

$$J(\omega_0) = J_0 + e|n_2 - n_1|\gamma_{12}(\omega_0)F_{ac}^2 \qquad (A16)$$

where only the frequency ω_0, saturating the system, appears. Here, we use the absolute value of the inversion, following our observation that the current also increases with absorption in the NEGF simulations, due to new transport channels opening up. The expression can readily be generalized to many modes of finite intensity, yielding a sum over field strengths at different frequencies ω_i, each with $\gamma_{12}(\omega_i)$. Identifying the gain in the expression for current, using Eq. (A14), gives

$$J^{fit}(F_{dc}, F_{ac}, \omega_0) = J_0 + ed|G_{12}(\omega_0)|\frac{c\epsilon_0\sqrt{\epsilon_r}F_{ac}^2}{2\hbar\omega_0}$$

$$= J_0 + ed|G_{12}(\omega_0)|\frac{I(\omega_0)}{\hbar\omega_0}, \qquad (A17)$$

where the total gain $G(\omega)$ contains a sum over the relevant transitions. The last factor in the first equation has been rewritten as the Poynting vector giving the intensity $I(\omega_0)$ at ω_0 in the final expression.

To map the NEGF simulation results onto the effective model, we first calculate J_0 and $G^0(\omega)$ for vanishingly small F_{ac} at each bias point $F_{dc}d$. We consider the range of 35–65 mV per module and frequencies 1.5–4.5 THz as relevant for domain formation. $G^0(\omega)$ is fitted by Δn_{21}^0 and $\gamma(\omega)$. According to Eq. (A15), the saturated gain can then be described by the effective lifetime $\bar{\tau}$, which is found from fitting the gain spectra to the NEGF simulations at higher intensities, as exemplified in Fig. 8(b). We thus require three fit parameters ($\Gamma, z_{21}, \bar{\tau}$), together with the calculated E_{21} and Δn_{21}^0 to model the saturated gain and current at each bias point. Here, the NEGF simulation data are fitted to a target function consisting of both Eqs. (A15) and (A17), which balances both the gain and stimulated current contributions and makes efficient use of all simulation data. The procedure provides a physically sound way of interpolating through the simulation data and allows us to calculate the current under irradiation as a function of bias, frequency, and ac field strength. Representative current and gain spectra are shown in Figs. 8(a) and 8(b), respectively, together with their fits using Eqs. (A17) and (A15).

Figures 8(a) and 8(b) show a particularly large linewidth for a bias of 50 mV per module. The reason can be seen in Fig. 6(b), where the lower laser level and the extraction level form a doublet with a spacing of 5 meV. Thus the gain is based on two different transitions of approximately equal strength, resulting in the large linewidth.

Unsaturated gain for a single module as a function of bias and frequency is displayed in Fig. 8(c). A strong Stark shift can be seen as bias is increasing. At the nominal operation point of 54 mV per module, gain peaks around 3.3 THz, which agrees with the experimental lasing frequencies reported in Ref. [17]; see also Fig. 5.

APPENDIX B: EXPERIMENTAL METHODS AND MEASUREMENTS

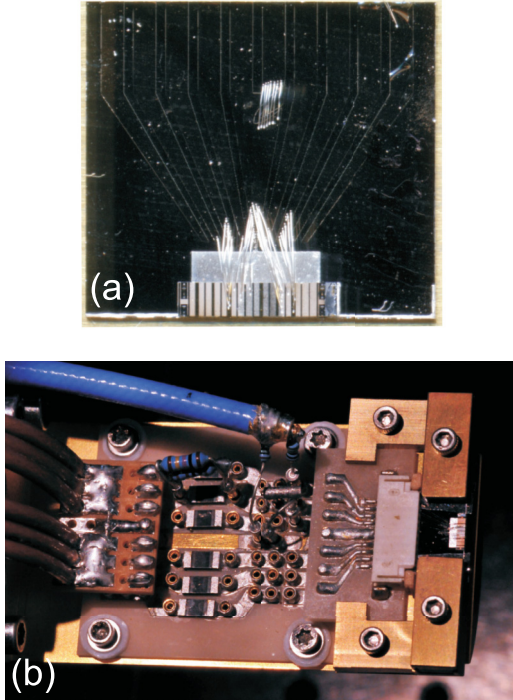We consider the structure V812 reported in Ref. [17] using devices processed with a Au-Au double metal waveguide.

FIG. 9. Cold finger inside the 10 K closed-cycle refrigerator: (a) Image of the TiAu metal-metal waveguide laser bar, 1049 μm long, soldered onto a high-resistive Si carrier. The fan-out electrodes deposited on carrier can be seen, but with a low contrast due to their small thickness; this is why they showed a residual resistivity. (b) The laser bar mounted on the cold finger. The blue wire is a 18-GHz SMA cable used for voltage detection and on the other side, it is connected to a 50-Ω input channel of a high-bandwidth oscilloscope. About 25 mm separate the laser bar from the SMA cable with, in between, a circuitry that is not optimized for RF.

These showed lasing up to the heat-sink temperature of 160 K. The laser under study, 1.049 mm long and 143 μm wide, is indium soldered onto a highly resistive ($>10^4$ Ω cm) hyperpure floating zone Si carrier on which fan-out Au electrodes were fabricated; see Fig. 9(a). Laser devices and simple mesas (nonlasing) with Pd/Ge/Ti/Pt/Au Ohmic contacts were also fabricated and mounted on a Si carrier.

Regrettably, both lasers, TiAu and PdGe contacted, were mounted on carriers with thin electrodes that showed residual, although non-negligible, resistance. The effect of the ground electrode resistance on measurements could not be circumvented easily, at least not in pulsed mode operation. Fortunately, the PdGe mesa devices were mounted on a carrier with much thicker electrodes (hence their vanishing resistance) and their electrical $J_{\text{mesa}} - U_{\text{mesa}}$ characteristics served as reference in order to derive the ground electrode resistance of the Si carrier, the Schottky barrier (for TiAu only), and therefore the exact bias per module on laser devices [Fig. 2(a)]. Consequently, in Fig. 2(a) the experimental average bias per module for the PdGe contacted mesa device is simply given by the signal from the voltage probe divided by $N = 222$. This is in contrast with lasing devices, where the potential drop across the ground electrode resistance of ~1 Ω (TiAu, dashed green) and ~0.85 Ω (PdGe, dashed purple) of their "defective" Si carrier, as well as

the Schottky top contact drop of 0.65 V for the TiAu device, had to be taken into account. It is worth mentioning that the PdGe mesa device was tested in voltage-controlled conditions, i.e., with a small load resistance $R_L = 5$ Ω, which could explain why the current plateaus are not very flat [Fig. 2(a), purple solid line]. In Figs. 2(b), 3(a), 3(c), and 3(e), the "raw" QCL voltage is not corrected from the effects of Schottky barrier and ground electrode resistance of Si carrier; the latter is likely to be temperature dependent. This explains to a large extent the difference between the vertical scales of Figs. 2(b) and 2(c). Nevertheless, the overall good agreement between theoretical and experimental biases per module can be appreciated in Fig. 2(a).

High-precision L-U_{QCL}-J characteristics were recorded using current controlled conditions, by use of a series resistance of $R_L = 41.2$ Ω placed near the device in a 9 K closed-cycle He refrigerator system; see Fig. 7(a) for the circuit. The external bias U_0 is supplied to the circuit by a pulse generator. The total current in the circuit, I_{tot}, was measured at the output port of the pulse generator with a calibrated 200-MHz bandwidth current transformer. Because of the highly resistive Si carrier, the device is operated with a floating ground. We checked that the net current in the 50-Ω coaxial cable from the voltage pulser is zero, meaning the current flowing in the QCL returns to the pulser ground via the shield of coaxial cable.

The voltage across the QCL, U_{QCL}, is recorded via a four-point measurement setup and with a calibrated voltage probe placed inside the cryostat and terminated to 50 Ω on the oscilloscope. The probe consists of a 18-GHz bandwidth subminiature version A (SMA) cable on which small-footprint 1000- and 330-Ω resistors were tightly soldered to center conductor and shield respectively. Despite the high-quality SMA cable used here, the RF performance of the voltage measurement setup is hindered by the absence of RF design between the input port of the voltage probe and the device, which are ~25 mm apart; see Fig. 9(b). Before reaching the voltage probe, the RF signal has to propagate through simple wire bonds connecting the QCL electrodes and the tip of fan-out electrodes patterned on Si, then through non-RF designed fan-out electrodes on the Si carrier, then conductors on two aluminium nitride boards, and finally the resistors used for the voltage probe. This incomplete RF design results in a ringing effect that is partially filtered out in Appendix E. In the future, a proper RF designed setup to probe the QCL voltage should be considered.

The small bypass current in the voltage probe [see Fig. 7(a)], I_{R_p} was subtracted in the final reported results of current density in Fig. 2(b), $J \equiv (I_{\text{tot}} - I_{R_p})/A$ in dc mode, and its resistance, R_p, was taken into account in the load curve that is explained with Eq. (A3) in next section; see also Fig. 7(a). The total circuit current I_{tot} and the QCL voltage U_{QCL} were measured in pulsed mode with 2-μs pulses, repeated at 100-Hz frequency and with 14-Hz macromodulation of the train of pulses to adapt the measurement to the response time of the Golay cell, the THz detector. The output of the Golay cell was connected to a lock-in amplifier with 1-s time constant and locked to 14-Hz reference signal. Here, unusually long pulses were used to benefit from the flatness of these pulses in their second half and consequently reported with high-accuracy data and longer sections of oscillations when they occur. Small heating effects on the laser threshold have been identified and

found to be responsible for vertical (U_{QCL}) shift of the merlon for long pulses, with the shift depending on the position of integration window where current and voltage are monitored. Experimentally, we observed the merlon at lower bias, if shorter pulses are applied (about 0.1 V lower for 300-ns pulse duration). This is why the electrical characteristics [Figs. 2(a) and 2(b), for instance] were recorded near the center of the 2-μs pulse, not close to the trailing edge. A 5-GS/s, 1-GHz bandwidth digital oscilloscope (Tektronix DPO4104) was used to measure the top of the pulses I_{tot} and U_{QCL} by using appropriate dc offsets and vertical scales. The I_{tot} and U_{QCL} values were measured inside a 200-ns-long integration window defined between cursors placed at $t = 1.08\,\mu$s and $t = 1.28\,\mu$s inside the pulse. Sixty-four current and voltage traces were averaged (average mode of oscilloscope) and finally reported with 1- and 2-mV/div scales, respectively, meaning that any changes of vertical scale that can result into discontinuities were taken into account and thoroughly corrected. Before turning on the average mode on the oscilloscope, clipping the single-pulse signals (observed in sample mode) by the 10-division vertical dynamic range was carefully avoided in the integration window (only). The calibration of the pulse generator was also checked as well as that of the oscilloscope. Data from oscilloscope and lock-in amplifier were recorded 32 times, 1 s apart, and finally means and standard deviations were derived. We used 50-mV voltage steps on the pulse generator in order to resolve features on the merlon. At each step, we also recorded 200 single traces, i.e., nonaveraged (sample mode), of I_{tot} and U_{QCL} channels to capture any oscillations or discontinuities. The median value of peak-to-peak amplitude of these pulses was computed inside the same 200-ns window of interest. Moreover, this median value was subtracted from the peak-to-peak amplitude of 64-pulse averaged signal to account for imperfect flatness of voltage and current channels in the integration window. After this subtraction, the final value was named the "net" amplitude, which is shown for the entire temperature range in Fig. 3(a) superimposed on the bias signal as shaded regions. Note that these amplitudes are only qualitative due to the limited bandwidth of the oscilloscope used here. When voltage oscillations were detected, current oscillations were also observed, although they were less intense due to limited bandwidth of current transformer.

The time-resolved voltage oscillations were recorded with a 40-GS/s 15-GHz bandwidth real-time oscilloscope (Tektronix TDS6154C) and a 10-dB attenuator was employed due to the large oscillation amplitude in region III. The first set of measurements with the 1-GHz oscilloscope permitted us to locate the oscillations with a low vertical resolution as a function of external bias. With the help of these low-resolution "spectra," we drove the time-resolved measurements with TDS6154C for different external biases and temperatures; single pulses were sampled at a maximum resolution of 25 ps/point.

Because of the residual positive slope of the external bias from the pulser (U_0), single-pulse measurements could reveal several sections of the merlon at once (such as regions III and IV). This simple technique, described in Appendix D, was convenient to assess the oscillating frequency versus raw QCL voltage.

The spectral measurements were performed with a continuous scanning Fourier transform infrared (FTIR) spectrometer set at a mirror velocity speed of 0.05 cm/s and resolution of 0.1 cm^{-1} and equipped with a LHe-cooled Si bolometer. We used a double modulation technique in which the QCL was biased with 0.5-μs pulses at a repetition rate of 300 Hz. The signal from the bolometer was filtered with a high-pass 200-Hz filter and finally sent to lock-in amplifier with time constant of 10 ms. Only five or ten scans were accumulated by FTIR.

In passing, we also note that high-resolution x-ray diffraction measurements indicate that the experimental layers are 1.7% shorter. For thinner wells, the tunnel resonances are shifted to larger biases and the lasing transitions to higher frequencies, which might account for some minor discrepancies observed between theory and experiment.

APPENDIX C: ADDITIONAL MODELING RESULTS

To complement the data shown in Fig. 4, a set of plots detailing the domain formation simulation results are shown in Figs. 10–13. They describe the simulated oscillations from just before threshold to a highest current density of 1.07 J_{thr}, corresponding to a change in external bias, U_0, from 54.2 to 57.8 V, respectively. At the high end of the current, see Figs. 13(g) and 13(h), the lasing is stabilized in the sense that the high-field domain always stays close to 50 mV per period and the laser action is uninterrupted. Increasing the external bias further, this state will eventually merge with the homogeneous branch as shown in Fig. 2(a).

Figure 10 focuses on the oscillating domains of region I. Here the oscillation frequency is slowly increasing with bias as the new instability occurs at a larger extent of the previous high-field domain. Thus, the accumulation front travels a shorter range, resulting in the frequency increase with U_0. The Fourier transforms (FTs) in the right-hand column were taken over a long signal (200 ns) compared to short stretch of time of only 20 ns used for the voltage and module color plots on the left side. In each of the panels, the frequency of the strongest oscillating signal is given together with the lowest frequency distinguishable in brackets. In panels (e) and (g), the threshold is actually reached for short periods in time, but the lasing field is too weak to influence the local current-field relation. Thus, the high-field domains keep the field strength of ∼62 mV per module.

Figure 11 shows the transition from region I to region II, where the lasing strongly increases and affects the high-field domains, whose fields drop. Because of the Stark shift, this implies a drop in lasing frequency, and lasing is now also observed for lower frequencies; see also Fig. 5. However, lasing stops after the high-field domain has shrunk sufficiently due to the traveling accumulation front. On the right-hand side, we note an increase in the oscillation frequencies.

The next collection of plots in Fig. 12 shows region III and the transition to region IV. Here the lasing is still active, while some new high-field domains form with a field of ∼50 mV per module, i.e., close to the NOP. Thus, two different domain formation scenarios coexist. These do either arrange in a pattern such as in Figs. 12(a), 12(b), 12(e), and 12(f) with subharmonic frequencies $f/3$ and $f/6$, respectively, or become irregular, as seen in Figs. 12(c) and 12(d). A similar subharmonic feature could also be detected experimentally; see Figs. 16 and 17(b) below. Within region III, where the average
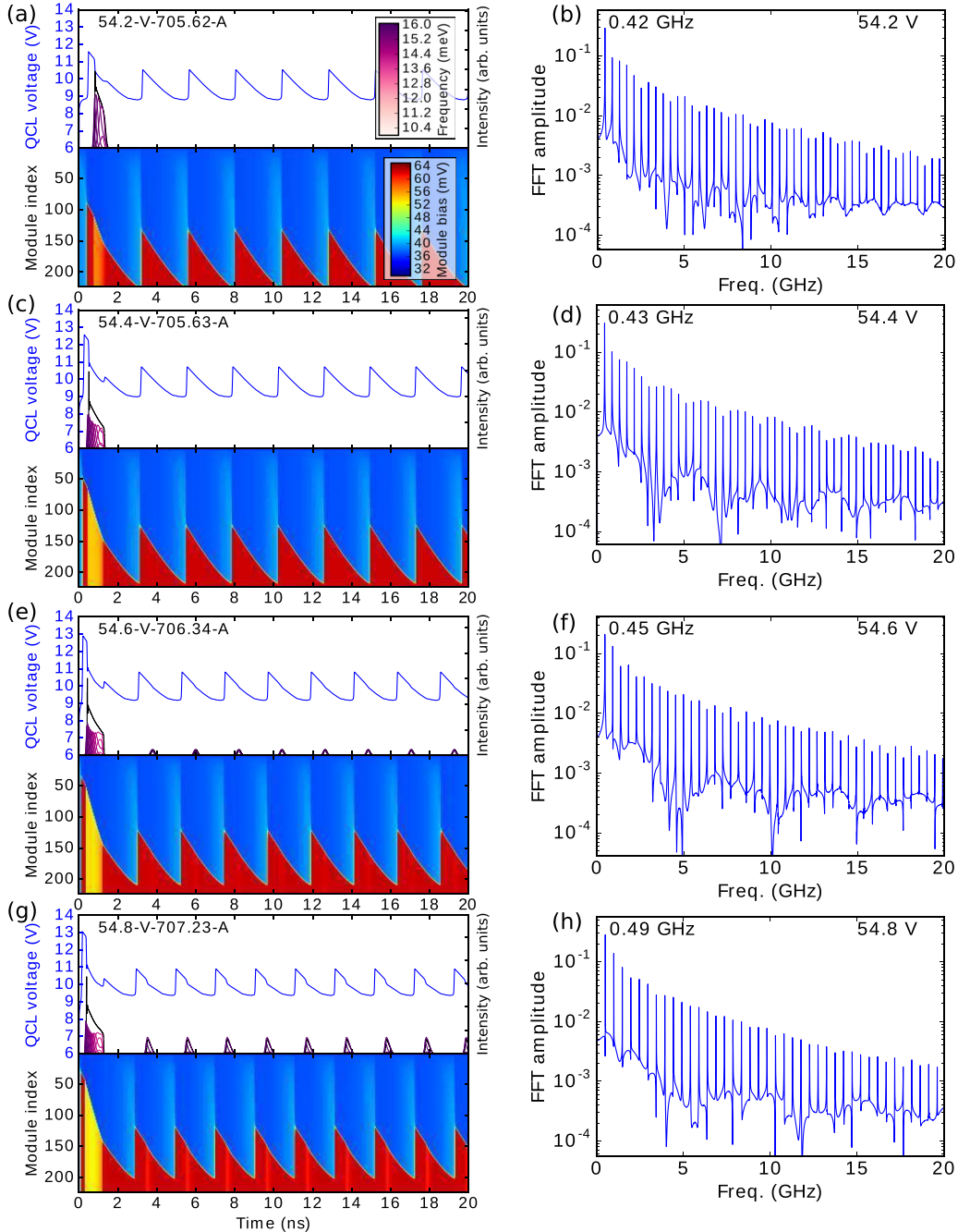
FIG. 10. Traveling domains simulations for external biases 54.2–54.8 V as indicated in the panels to complement the data in Fig. 4. The color bars in the top and bottom panels of the left section apply also to the rest of the column, where they have been removed for increased clarity. Fast Fourier transforms (FT) of the simulated voltage oscillations $U_{QCL}(t)$ are shown with matching external bias in the right column. The voltage oscillations for the FT were recorded over a sample time of 200 ns. In each such panel, the frequency of the strongest harmonic is indicated.

bias drop over the QCL is roughly constant, less than half of the new high-field domains exhibit this low field. For the lowest panels [Figs. 12(g) and 12(h)], the two different domain formation processes alternate. For this operation point, the average bias reaches a maximum, defining the transition to region IV.

In the final collection of plots in Fig. 13, decreasing oscillation frequencies of region IV can be studied, where the interruptions in lasing become less frequent. As field domains

with high field become rare, the average bias drops in this region upon increase of the total bias U_0, which defines region IV. In the lowest panels [Figs. 13(g) and 13(h)], the lasing is uninterrupted and region V is reached, where the laser operates with a linear increase of bias and intensity with current. Our simulations show some oscillatory feature. However, the amplitude of the bias oscillation is strongly reduced compared to the other regions.
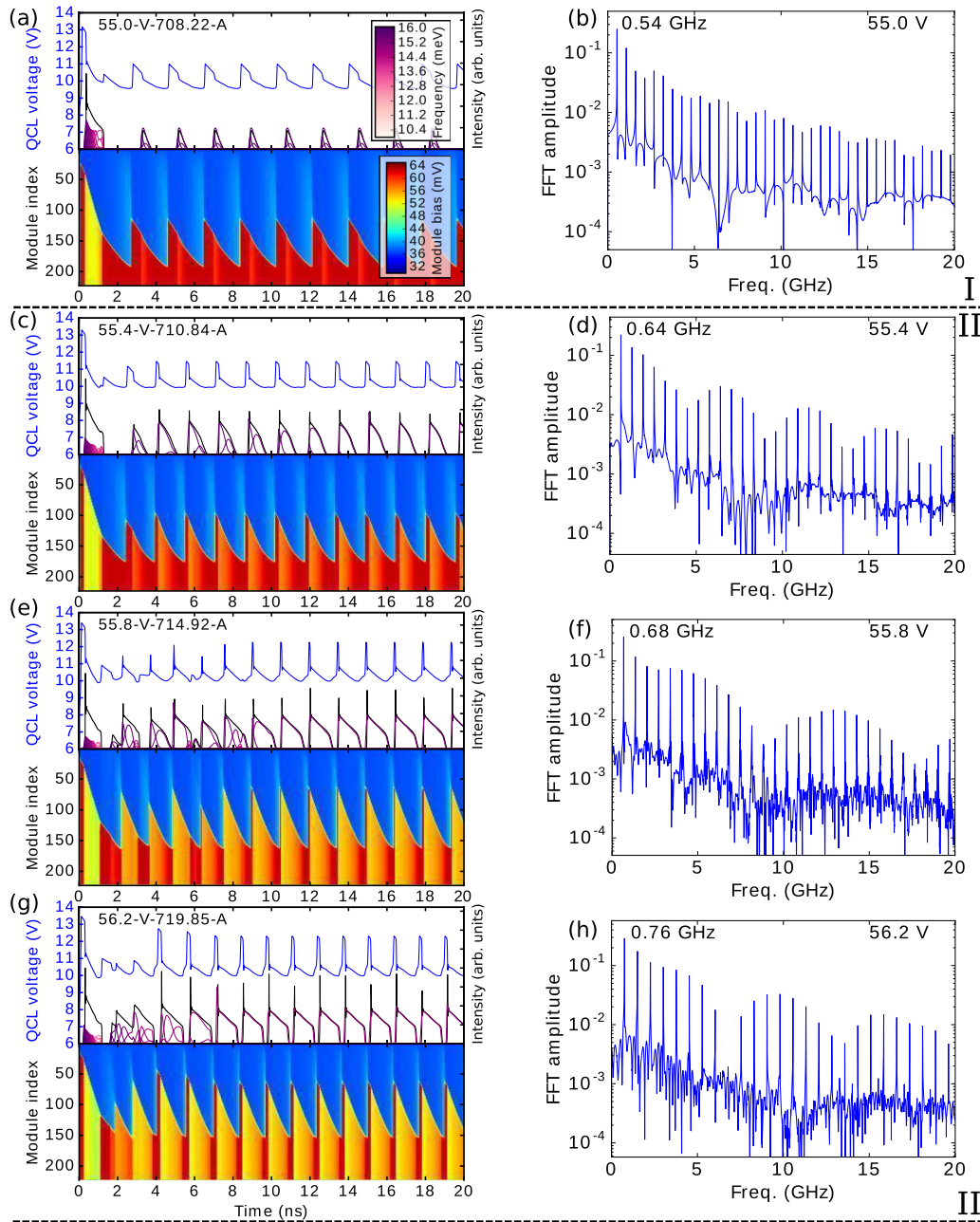
FIG. 11. Traveling domains simulations for external biases 55.0–56.2 V as indicated in the panels to complement the data in Fig. 4. The color bars in the top and bottom panels of the left section apply also to the rest of the column, where they have been removed for increased clarity. Fast Fourier transforms (FT) of the simulated voltage oscillations $U_{QCL}(t)$ are shown with matching external bias in the right column. The voltage oscillations for the FT were recorded over a sample time of 200 ns. In each such panel, the frequency of the strongest harmonic is indicated.

APPENDIX D: BIAS DEPENDENCE OF OSCILLATION FREQUENCY

The voltage dependence of the oscillation frequency can be demonstrated by repeating the measurement of the raw QCL voltage with the 15-GHz bandwidth oscilloscope at different external biases U_0. However, this obvious measuring technique was hampered by the pulse-to-pulse variations. Therefore, a faster method was also employed which relied on the residual positive slope of the voltage input pulse and a local Fourier transform within a Gaussian window covering ∼40 ns. This

slope is non-negligible for $t < 1 \mu$s and is greatly reduced at longer time as the external bias eventually converges to the set-point value.

In the set of experiments reported in Appendixes D and E, we actually used a different device than the one in Secs. II and III. This device is from the same laser bar, mounted on the same Si carrier, and its electrical characteristics (the merlon, for instance), are very similar. However, the bias oscillations were stronger with a peak-to-peak value up to 3.6 V as monitored by the 15-GHz bandwidth oscilloscope.
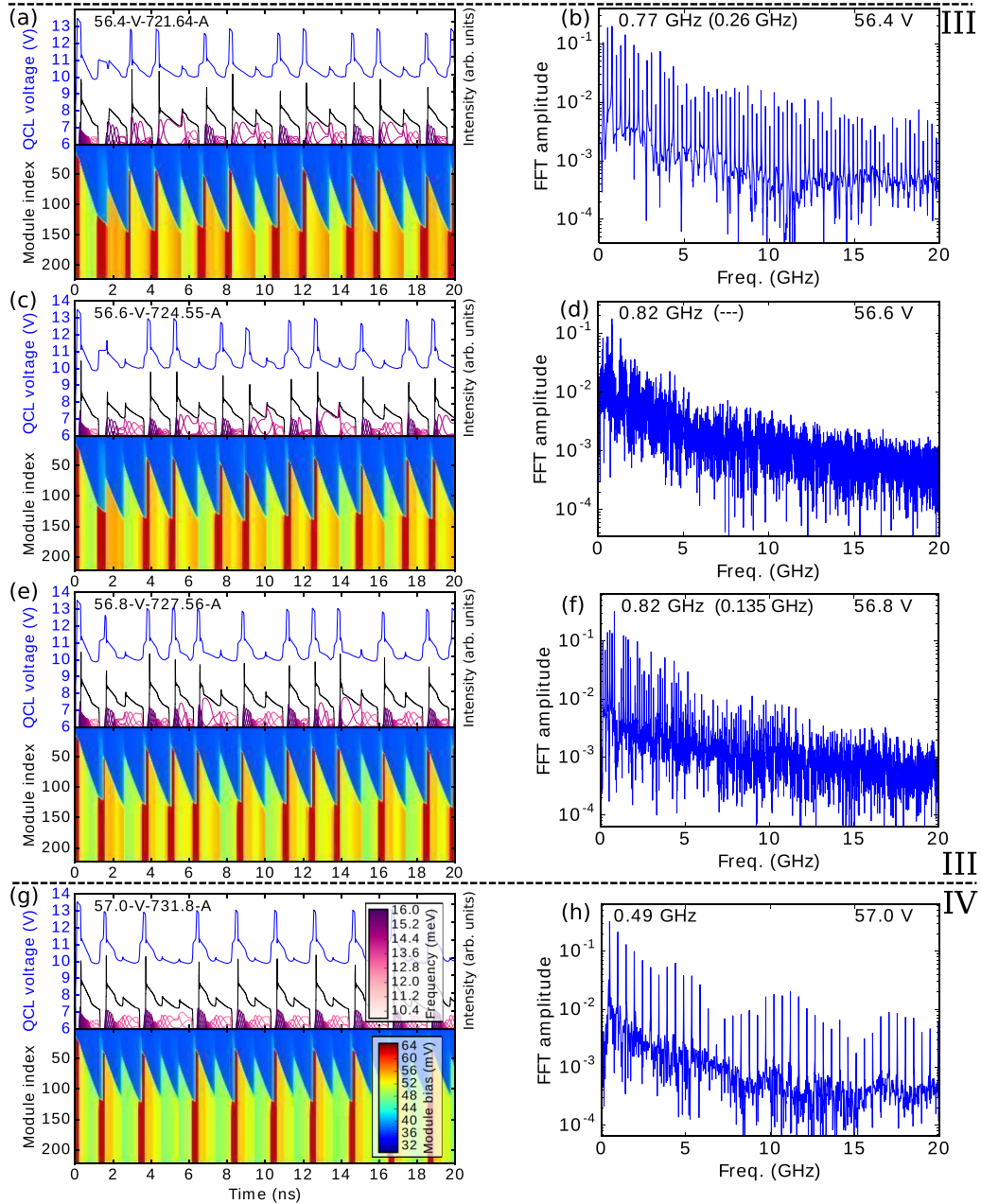
FIG. 12. Traveling domains simulations for external biases 56.4–57.0 V as indicated in the panels to complement the data in Fig. 4. The color bars in the top and bottom panels of the left section apply also to the rest of the column, where they have been removed for increased clarity. Fast Fourier transforms (FT) of the simulated voltage oscillations $U_{\mathrm{QCL}}(t)$ are shown with matching external bias in the right column. The voltage oscillations for the FT were recorded over a sample time of 200 ns. In each such panel, the frequency of the strongest harmonic is indicated. If the fundamental frequency differs, its value is added inside brackets.

For the data reported here, we employed a 6.25-GS/s, 2-GHz bandwidth oscilloscope (Tektronix MSO58) with its 8-bit analog-to-digital converter to benefit from its maximum sampling rate. A digital low-pass filter with a cutoff frequency of 312.5 MHz was available, which allowed the real-time visualization of changes in average bias as characteristic for different regions in the merlon. By carefully adjusting the set point on the pulser, we could observe the oscillations in region I with the transition to region II [see Fig. 14(a)], as well as the oscillations in region III with the transition to region IV [Fig. 14(b)]. Fine-tuning of the pulser set point and

a "judicious" choice of the pulses—due to inevitable pulse-to-pulse fluctuations—were necessary to obtain this data.

Figure 14 shows two examples of oscillations at 9 K for external bias corresponding to regions I [nominal pulse amplitude $U_0 = 55.24$ V, Figs. 14(a) and 14(c)] and III [$U_0 = 57.90$ V, Figs. 14(b) and 14(d)]. Figures 14(a) and 14(b) are the oscilloscope screen captures of the total current pulse (magenta), the raw QCL voltage (green), and the low-pass filtered voltage (orange). Figures 14(c) and 14(d) show the results of a moving Fourier analysis performed on the raw QCL voltage. For that purpose, 45-ns-wide [Fig. 14(c)] and
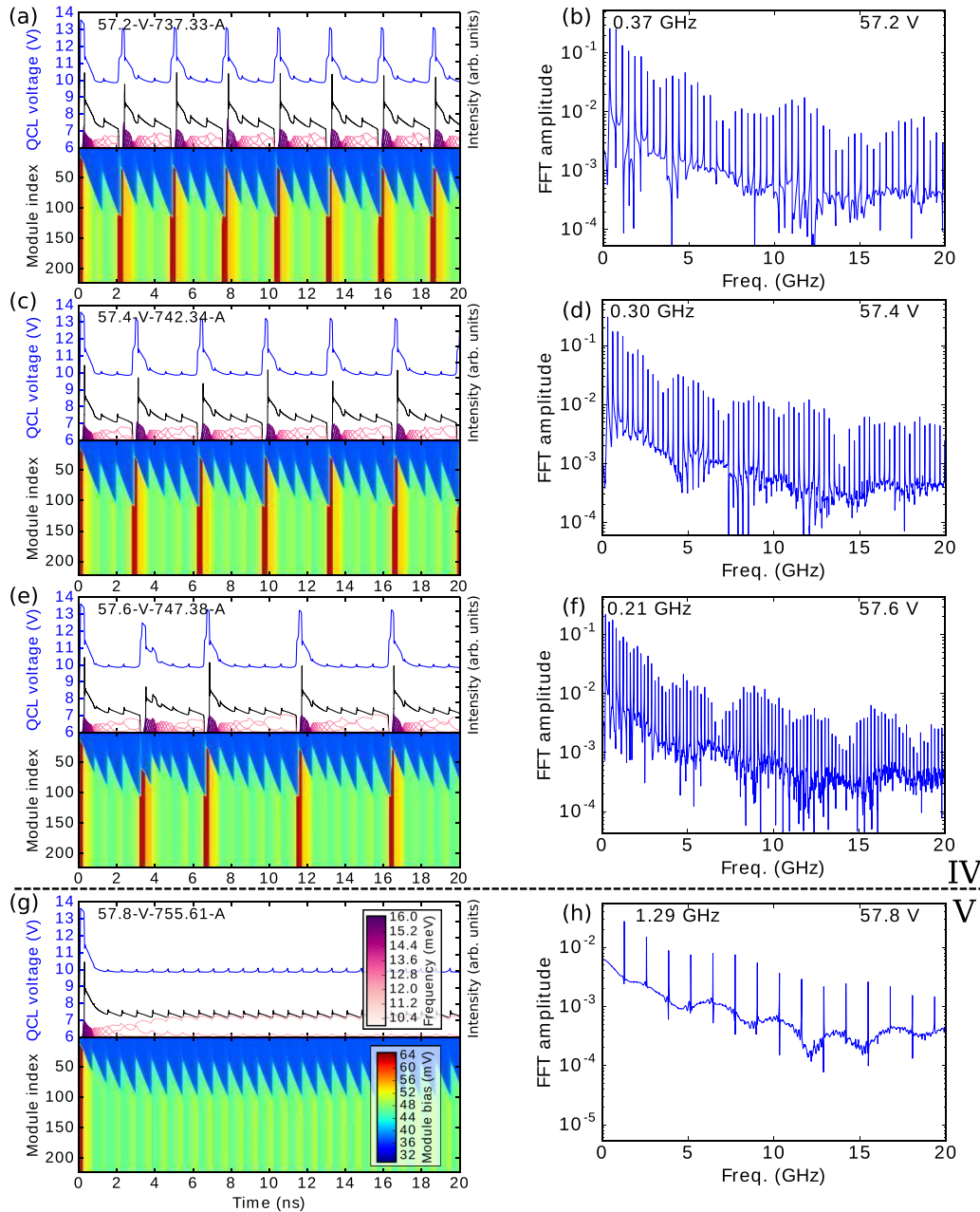
FIG. 13. Traveling domains simulations for external biases 57.2–57.8 V as indicated in the panels to complement the data in Fig. 4. The color bars in the top and bottom panels of the left section apply also to the rest of the column, where they have been removed for increased clarity. Fast Fourier transforms (FT) of the simulated voltage oscillations $U_{\mathrm{QCL}}(t)$ are shown with matching external bias in the right column. The voltage oscillations for the FT were recorded over a sample time of 200 ns. In each such panel, the frequency of the strongest harmonic is indicated.

40-ns-wide [Fig. 14(d)] Gaussian windows with center shifted from the leading to the trailing edge of the pulse were used. The standard deviations of the Gaussians were 7.5 and 6.7 ns respectively. By doing so, in a single shot, the average voltage within the Gaussian window (black line) can be computed and the voltage sensitivity of the first harmonic frequency (purple line) estimated, although the nonflatness of the external bias pulse might slightly influence the oscillation frequency.

In Figs. 14(a) and 14(c), we identify the transition between regions I and II at $t \approx 0.65$ μs by the sudden change in slope in

bias, which stops its strong increase. In more detail, the inset of Fig. 14(c) displays a small spike in bias ($\sim$10 mV), similar to the one observed at threshold for low temperatures in Fig. 2(b) where the spike is $\sim$20 mV in average mode. Furthermore, a slight increase in the current slope also indicates the transition to a region with higher average conductivity as common for region II due to lasing. These features are similar for all pulses analyzed. Regarding the lasing signal, we observed that the phase of the lock-in amplifier starts to be stabilized, when the oscillations vanish at the end of the pulse (strictly speaking for the majority of pulses with nominally equal set point bias U_0).
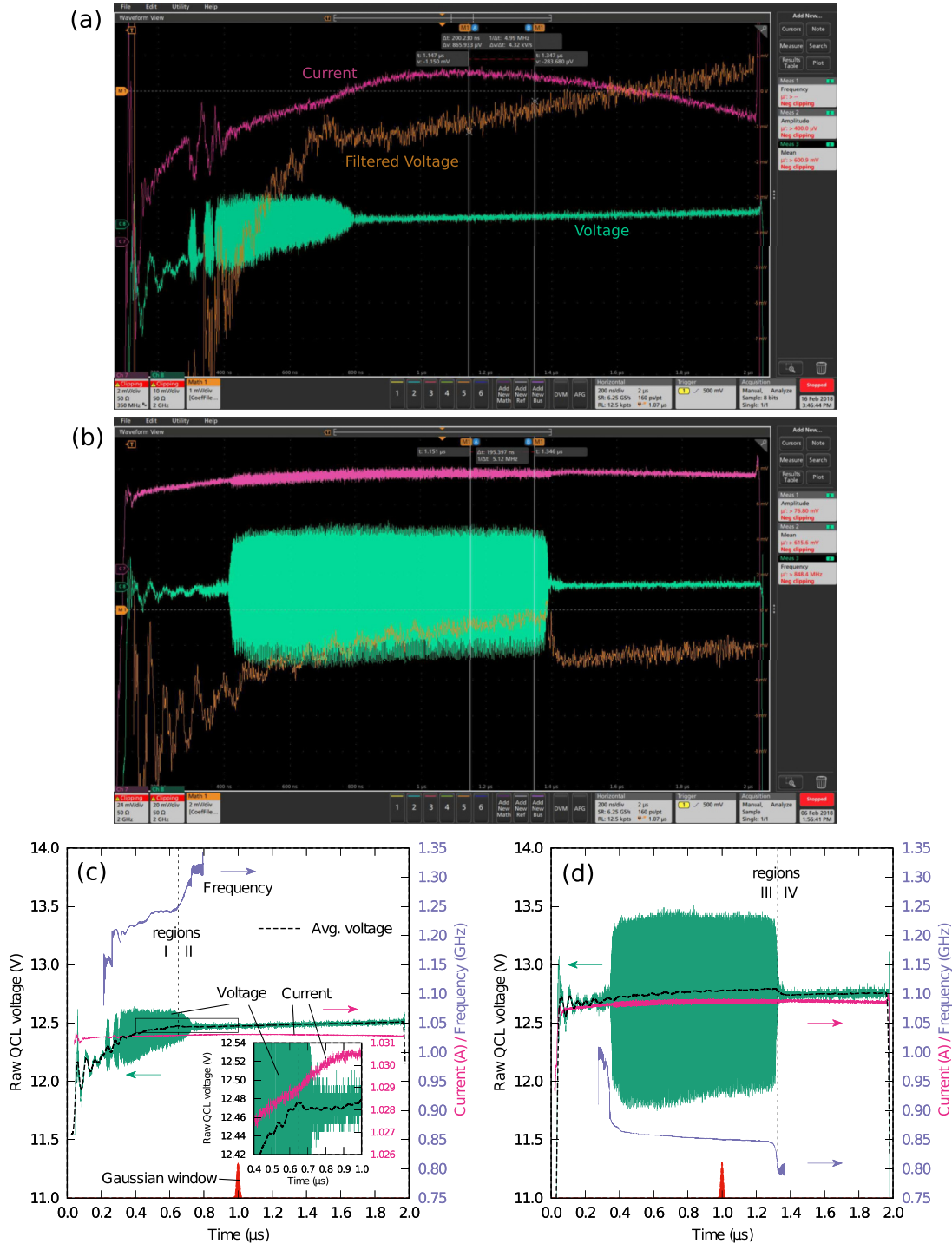
FIG. 14. Time-resolved oscillations at 9 K over the 2-μs-long pulse with a residual positive slope as measured with a 2-GHz bandwidth oscilloscope. Panels (a) and (b) are screen captures of the oscilloscope for $U_0 = 55.24$ V (i.e., around lasing threshold) and $U_0 = 57.9$ V respectively. As also indicated in panel (a), the magenta trace represents the current (I_{tot}) pulse, the green trace is the raw QCL voltage, and the orange trace shows the QCL voltage channel with a 312.5-MHz low-pass filter. The sharp step down on the filtered voltage in panel (b) illustrates the right side of the merlon, region IV, previously recorded in average mode [see Fig. 2(b)]. Panels (c) and (d) provide a detailed analysis of the data from panels (a) and (b), respectively. The purple curve (labeled *Frequency*) represents the instantaneous first harmonic frequency computed within a moving integration window, which is represented by a filled red curve (labeled *Gaussian window*) at the bottom. The dashed black line represents the voltage averaged within the Gaussian window. The inset in panel (c) focuses on the identification of threshold, the boundary between regions I and II, at $t \approx 0.65\,\mu$s: (i) The average slope of the QCL voltage decreases; (iii) the average slope of the QCL current increases slightly; and (iii) the voltage exhibits a tiny spike of 10 mV at $t \approx 0.65\,\mu$s, similar to Fig. 2(b) at threshold (where 20 mV is observed in average mode). The vertical dashed lines represent region boundaries, which we could clearly identify. The slow decline of current and increase of average voltage for $t \gtrsim 1.3\,\mu$s are attributed to sample heating.
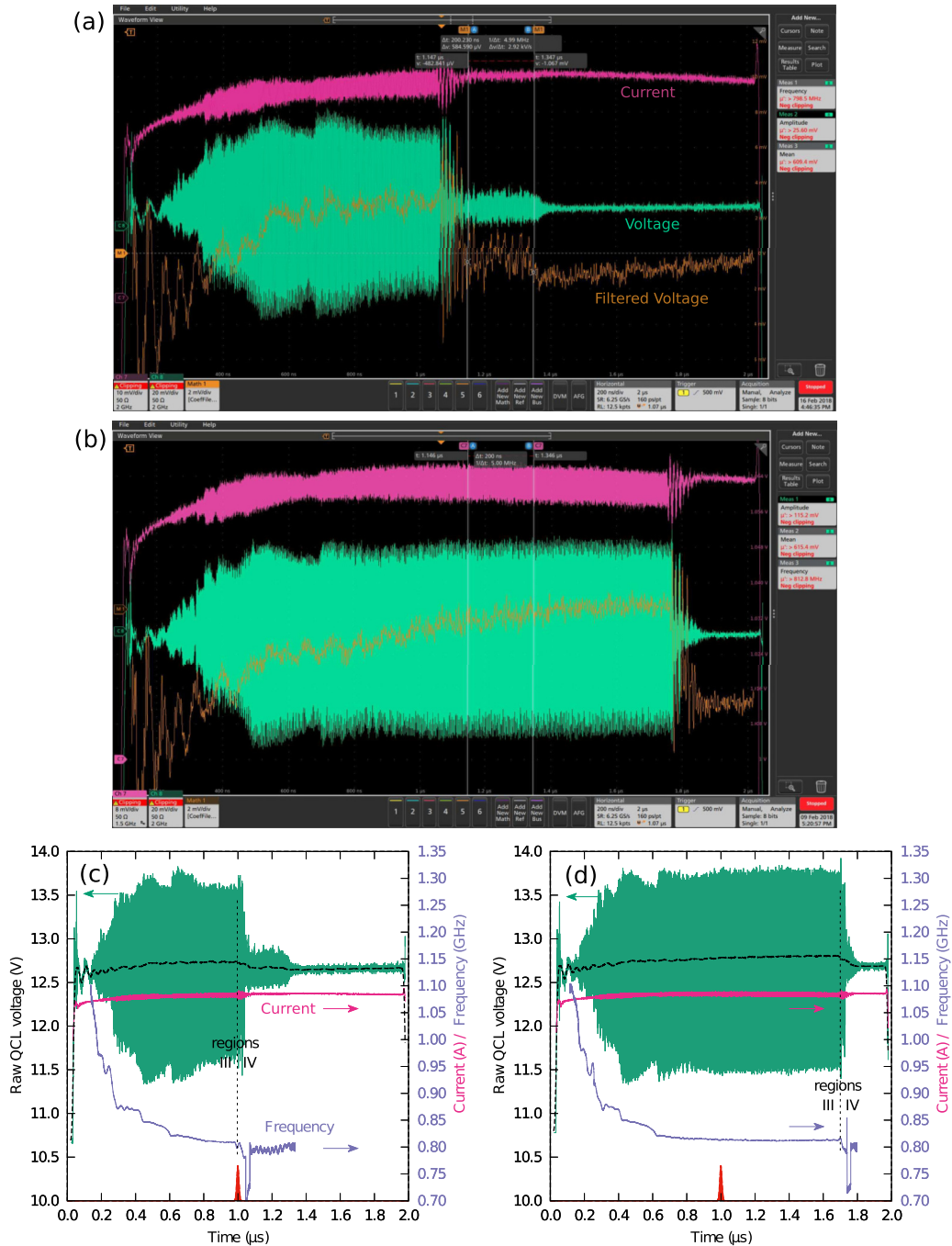
FIG. 15. Time-resolved oscillations recorded with the 2 GHz oscilloscope at 9 K and $U_0 = 57.76$ V for two different pulses. All curves correspond to Fig. 14. The deviations between panels (a), (c) and (b), (d) show typical pulse-to-pulse fluctuations. In both cases a multi-segment region III and an instantaneous oscillation frequency evolving like a staircase are observed. The ~0.1 V drop of average voltage (dashed black line) marks the region IV, the right side of merlon in Fig. 2(b).

Figure 14(c), which is representative for many pulses analyzed, shows that the oscillations are decaying in time after entering the region II. This relates the transition between regions I and II with threshold; see also Fig. 2(b). Therefore, laser threshold occurs in a state of running electric field domains, a likely hypothesis that could be confirmed with a fast THz detector [30]. Consequently, for $t < 0.65$ μs the device is operated in region I, where we observe oscillations with a peak-to-peak amplitude of ~0.4 V and frequencies of ~1.2 GHz, slightly

increasing with bias. These values agree well with the data in Figs. 3(b) and 3(c), where a different device was studied with a 15-GHz oscilloscope.

In Fig. 14(b), the sharp drop of filtered voltage (orange) indicates region IV, the only region where the bias over the QCL drops. This allows the identification of region III for times $t < 1.3$ μs; see also Fig. 14(d). Within this region, large-amplitude voltage oscillations with peak-to-peak amplitude of ~1.8 V and a frequency of ~0.85 GHz, decreasing with
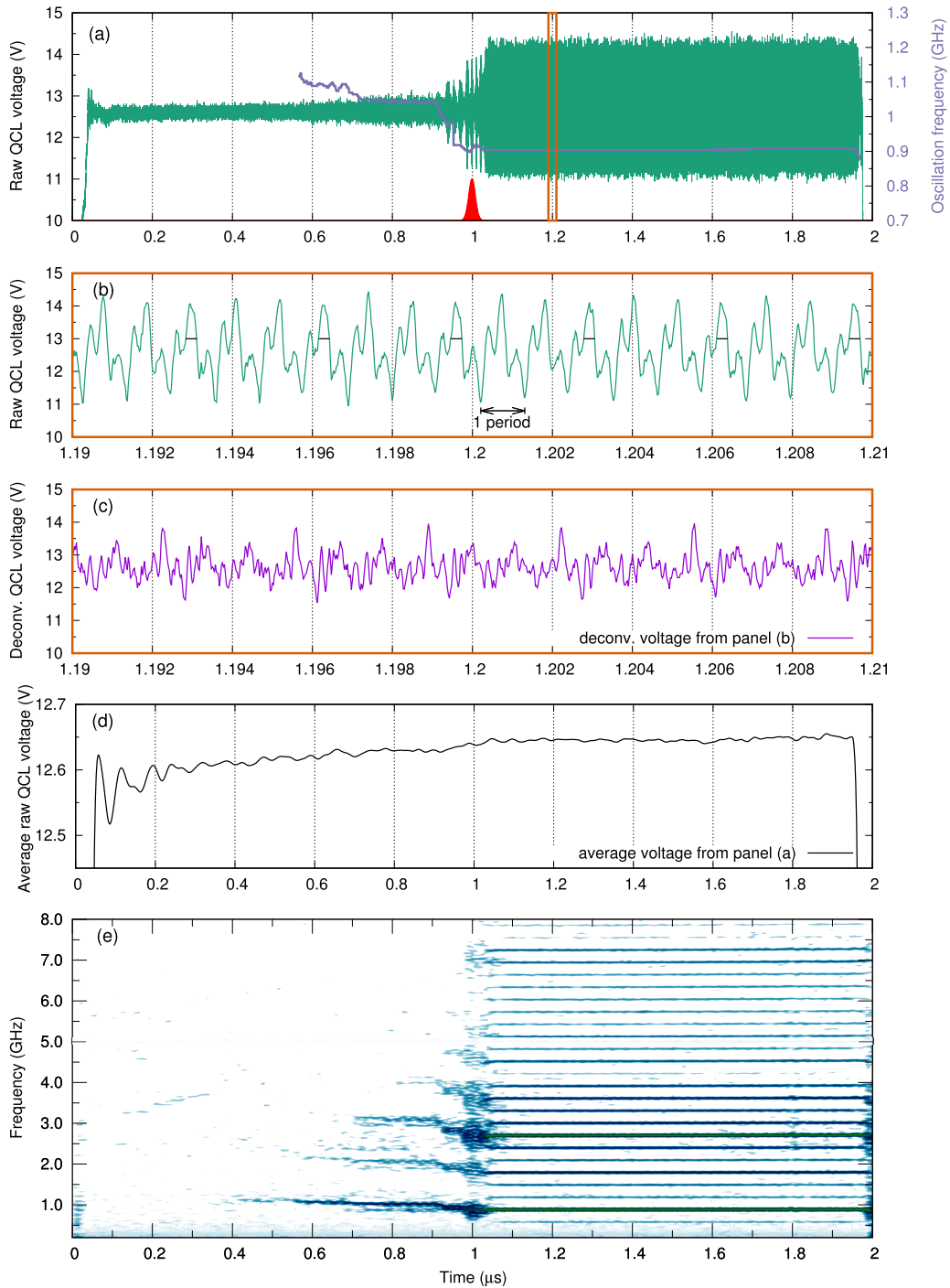
FIG. 16. Time-resolved oscillations recorded with the 15 GHz oscilloscope at 9 K and $U_0 = 57.54$ V for a pulse with good stability. Panel (a), left axis, shows the top of the 2-μs long pulse of the raw QCL voltage. The right axis is the instantaneous frequency as computed within a 50-ns wide Gaussian window with 8.5-ns standard deviation displayed around $t = 1\,\mu$s. Panel (b) shows details of the recorded bias signal in a 20-ns wide window. The dominant frequency of 0.9 GHz corresponds to the period indicated. However, by looking into more detail, only one of three periods are identical, as it can be seen by the wider peaks marked with a black bar. Panel (c) shows the same 20-ns wide window after filtering out the ringing effects. Panel (d) shows that the $f/3$ subharmonic regime is observed when the average raw voltage is stabilized at ≈ 12.65 V. Panel (e) shows the instantaneous frequency spectrum.

bias, are detected by the 2-GHz oscilloscope (with the 15-GHz oscilloscope higher amplitudes are resolved). These values are again comparable to Figs. 3(d) and 3(e). The oscillations are also echoed in the current signal despite the current transformer being limited to a 200-MHz bandwidth. We observe that this region is very sensitive to the bias pulses, as shown in Fig. 15. The envelope of oscillations varies greatly from pulse to pulse and we see variations from day to day. Nevertheless, the key

issues are pertinent: (i) the giant amplitude of oscillations of several volts, (ii) the oscillation frequency consistently in $\sim$850-MHz range,[3] and (iii) an averaged voltage drop $\sim$0.1 V within region IV. While the voltage drops, the oscillations actually persist, albeit with reduced amplitude. This is best seen in Figs. 15(a) and 15(c).

It is noteworthy that the pulse-to-pulse variations sometimes lead to a region III consisting of several segments with different amplitudes and with decreasing center frequencies; see Figs. 15(c) and 15(d). The moving FT results in an instantaneous frequency versus time that looks like a staircase, where the last step is centered at $\sim$813 MHz. When such a multisegment region III appears, it is also concomitant with a deeper average voltage step in region IV.

Analyzing the operation point with a raw QCL voltage of 12.65 V in region III in more detail with the 15-GHz oscilloscope, we could actually observe subharmonics $f/3$; see Fig. 16. For larger values of U_0, we observe this $f/3$ subharmonic regime systematically, when the QCL bias crosses the 12.65-V level.

APPENDIX E: FILTERING THE OSCILLATION PATTERNS BY DECONVOLUTION

For a better interpretation of the large-amplitude oscillations of the raw QCL voltage observed in region III [see Figs. 3(e) and 14–16], the step response of the voltage probe setup was measured by employing a 200-ps rise-time pulser. In that way, the setup was characterized up to $\sim$7 GHz. During this test, the load resistance R_L was removed and the bias setpoint $U_0 \approx 6$ V was chosen to match the 50-Ω dc impedance on the QCL at this bias. This measurement revealed a general ringing enveloppe at $\sim$0.93 GHz with a exponential decay of 1.1 ns, but also some complex features inside this envelope. From classic Fourier analysis, we could reconstruct an *estimated* impulse response of the voltage detection setup. The impulse response shows complex ringing effects that we could not associate with simple electrical circuits. This response lasts for $\approx$3 ns and it is peaked at $t = 0.75$ ns after the impulse. When integrating the impulse response, which is equivalent to derive the step response, the ringing effect would cause a strong 75% voltage overshoot at $t = 0.87$ ns. With such an impulse response and by employing standard Fourier analysis, we tried to perform deconvolution on the complex oscillation traces of the raw QCL voltage. Nevertheless, the results of this operation should be treated with cautious, considering (i) the RF circuit of the setup is far from optimized, as already explained in Appendix B and illustrated via Fig. 9 and (ii) our characterization technique is limited to $\sim$7 GHz so far.

Figure 17 shows the result of deconvolution for an external bias corresponding to region III. The span of oscillations does not last 2 μs because of the residual positive slope of the input pulse (see Appendix D). Figure 17(a) demonstrates a reduction of the peak-to-peak amplitude oscillation after deconvolution, suggesting the ringing effects have been filtered out to a large extent. The next three panels show 10-ns-wide enlarged areas representing segments, with different oscillation amplitudes in Fig. 17(a). From a bird's eye view, the raw QCL voltage patterns in the different segments look similar as ringing effects dominate; nevertheless, after deconvolution the differences become more evident. When the average voltage is $\sim$12.65 V, we systematically observed a $f/3$ subharmonic regime, where $f = 0.884$ GHz is the main oscillation frequency [Figs. 17(b) and 16]. The filtered trace seems to indicate there could be one strong "spike" of voltage once every three periods. Such complex oscillations with three different spikes in a $3/f$ lapse of time have been predicted by our model, see Figs. 12(a) and 12(b), and our filtered voltage trace resonates rather well with these simulations. Figures 17(c) and 17(d) show the filtered QCL voltage around $t = 0.88$ and $t = 1.64$ μs respectively. The average voltage and fundamental frequency are 12.66 V and 0.874 GHz respectively around $t = 0.88$ μs and 12.7 V and 0.850 GHz around $t = 1.64$ μs. These filtered traces display general square-like $\sim$0.5 V oscillations (with some high-frequency noise). In addition, these oscillations are the "pedestal" of voltage spikes that briefly appears at the end of the top plateaus of the square-like oscillations. From this filtering operation, the amplitude of the spikes could be as high as $\sim$1 V, suggesting that during a short period of time many modules are forming a high-field domain at a bias corresponding to the alignment of the upper lasing state with level 5. With cautiousness, one could state that the deconvoluted traces seem in rather good agreement with some simulated voltage traces [Figs. 4(b)–4(d) and 11–13]. When the same procedure is performed on oscilloscope traces recorded for an external bias corresponding to the birth of oscillations in region III, the spikes of voltage appear in the middle of the top plateau of the square-like oscillations.

When the filtering operation is performed on oscilloscope traces recorded for external biases set near threshold (end of region I, beginning of region II), the filtered and unfiltered signals have about the same amplitude oscillations, which suggests that the ringing effects did not affect the measurement very much. In this case, it seems that before threshold the oscillations pattern are triangular-like, and after threshold they become more square-like, an observation which is in resonance with simulations displayed in Figs. 10 and 11. Nevertheless, the signal to noise and the bandwidth limitation of the filtering operation prevent a solid confirmation of these preliminary observations.

To summarize, this deconvolution procedure indicates the severity of distortion in the measured signal and emphasizes the importance of better RF design of voltage detection setup; this would become even more crucial if chaotic behavior were investigated.

---

[3]The same $\sim$850-MHz oscillation frequency was automatically computed by the oscilloscope between the vertical cursors and displayed as "Meas 3" on the right side of the screen capture in Fig. 14(b).
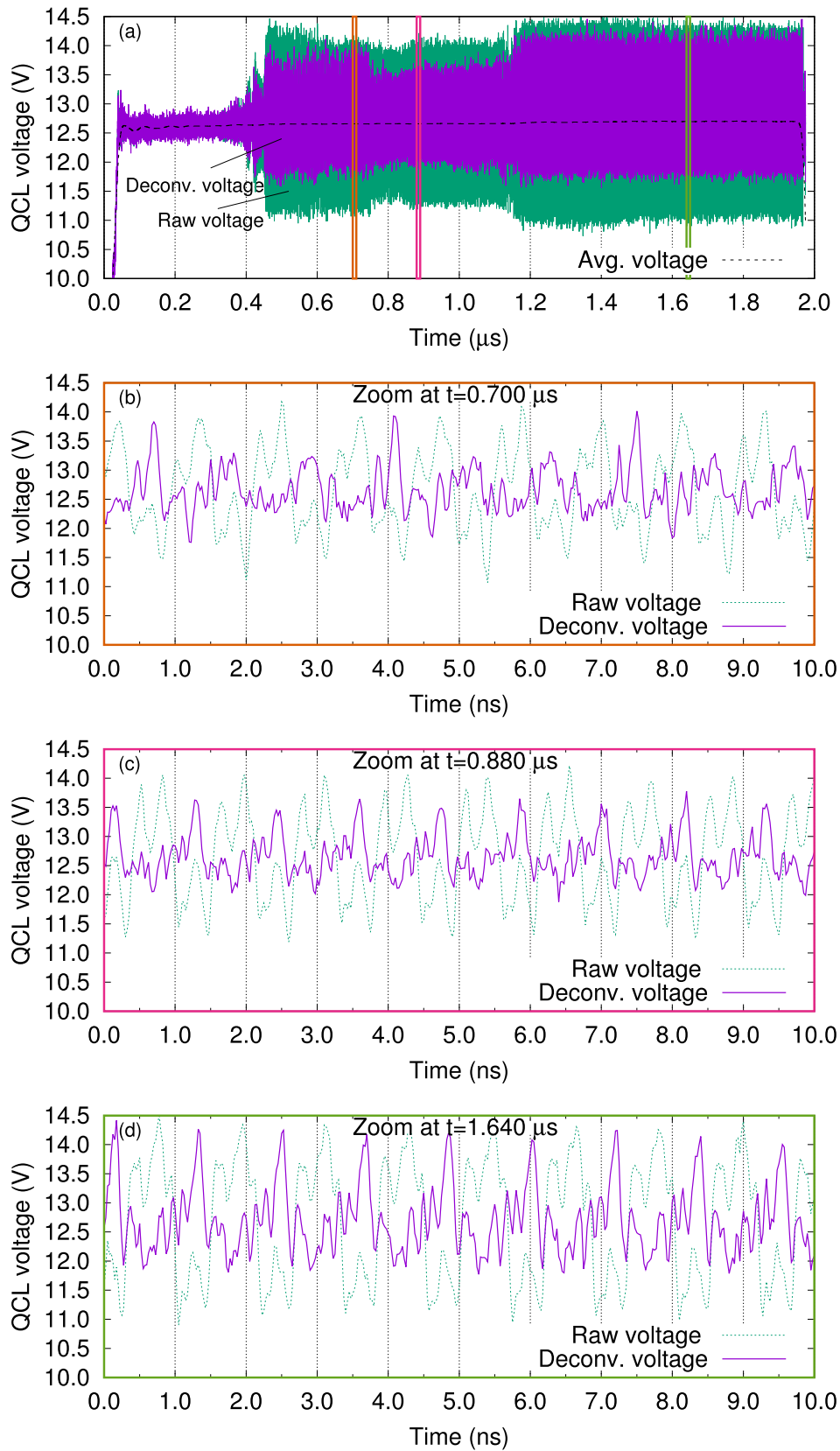
FIG. 17. Exemplary deconvolution of the time-resolved oscillations at 9 K and $U_0 = 57.65$ V: (a) The 2-μs-long green trace is the raw signal from the voltage probe recorded with a 15-GHz bandwidth oscilloscope and the magenta trace with lower amplitude oscillations is the result from deconvolution. The dashed black trace is the average voltage computed within a moving 50-ns-wide Gaussian average window (with 8.5 ns standard deviation). A multisegment region III of oscillations can be observed. Panels (b)–(d) represent three 10-ns-wide enlarged areas. Panel (b) corresponds to the $f/3$ subharmonic regime, which becomes more distinct after deconvolution.

[1] L. Esaki and R. Tsu, Superlattice and negative differential conductivity in semiconductors, IBM J. Res. Dev. **14**, 61 (1970).

[2] S. A. Ktitorov, G. S. Simin, and V. Ya. Sindalovskii, Bragg reflections and the high-frequency conductivity of an electronic solid-state plasma, Sov. Phys. Sol. State **13**, 1872 (1972) [Fizika Tverdogo Tela **13**, 2230 (1971)].

[3] H. Kroemer, Large-amplitude oscillation dynamics and domain suppression in a superlattice Bloch oscillator, arXiv:cond-mat/0009311.

[4] M. P. Shaw, V. V. Mitin, E. Schöll, and H. L. Grubin, *The Physics of Instabilities in Solid State Electron Devices* (Plenum Press, New York, 1992).

[5] L. Esaki and L. L. Chang, New Transport Phenomenon in a Semiconductor "Superlattice," Phys. Rev. Lett. **33**, 495 (1974).

[6] A. Wacker, Semiconductor superlattices: A model system for nonlinear transport, Phys. Rep. **357**, 1 (2002).

[7] L. L. Bonilla and H. T. Grahn, Nonlinear dynamics of semiconductor superlattices, Rep. Prog. Phys. **68**, 577 (2005).

[8] Y. Shimada, K. Hirakawa, M. Odnoblioudov, and K. A. Chao, Terahertz Conductivity and Possible Bloch Gain in Semiconductor Superlattices, Phys. Rev. Lett. **90**, 046806 (2003).

[9] P. G. Savvidis, B. Kolasa, G. Lee, and S. J. Allen, Resonant Crossover of Terahertz Loss to the Gain of a Bloch Oscillating InAs/AlSb Superlattice, Phys. Rev. Lett. **92**, 196802 (2004).

[10] J. Faist, F. Capasso, D. L. Sivco, C. Sirtori, A. L. Hutchinson, and A. Y. Cho, Quantum cascade laser, Science **264**, 553 (1994).

[11] J. Faist, *Quantum Cascade Lasers* (Oxford University Press, Oxford, UK, 2013).

[12] R. F. Kazarinov and R. A. Suris, Possibility of the amplification of electromagnetic waves in a semiconductor with a superlattice, Sov. Phys. Semicond. **5**, 707 (1971).

[13] S. L. Lu, L. Schrottke, S. W. Teitsworth, R. Hey, and H. T. Grahn, Formation of electric-field domains in GaAs/Al$_x$ Ga$_{1-x}$ As quantum cascade laser structures, Phys. Rev. B **73**, 033311 (2006).

[14] M. Wienold, L. Schrottke, M. Giehler, R. Hey, and H. T. Grahn, Nonlinear transport in quantum-cascade lasers: The role of electric-field domain formation for the laser characteristics, J. Appl. Phys. **109**, 073112 (2011).

[15] H. Yasuda, I. Hosako, and K. Hirakawa, High-field domains in terahertz quantum cascade laser structures based on resonant-phonon depopulation scheme, in *Proceedings of the 38th International Conference on Infrared, Millimeter, and Terahertz Waves (IRMMW-THz), Mainz* (IEEE, New York, NY, 2013), pp. 1–2.

[16] R. S. Dhar, S. G. Razavipour, E. Dupont, C. Xu, S. Laframboise, Z. Wasilewski, Q. Hu, and D. Ban, Direct nanoscale imaging of evolving electric field domains in quantum structures, Sci. Rep. **4**, 7183 (2014).

[17] S. Fathololoumi, E. Dupont, Z. R. Wasilewski, C. W. I. Chan, S. G. Razavipour, S. R. Laframboise, S. Huang, Q. Hu, D. Ban, and H. C. Liu, Effect of oscillator strength and intermediate resonance on the performance of resonant phonon-based terahertz quantum cascade lasers, J. Appl. Phys. **113**, 113109 (2013).

[18] S. Fathololoumi, E. Dupont, C. W. I. Chan, Z. R. Wasilewski, S. R. Laframboise, D. Ban, A. Mátyás, C. Jirauschek, Q. Hu, and H. C. Liu, Terahertz quantum cascade lasers operating up to ~200 K with optimized oscillator strength and improved injection tunneling, Opt. Express **20**, 3866 (2012).

[19] B. S. Williams, S. Kumar, H. Callebaut, Q. Hu, and J. L. Reno, Terahertz quantum-cascade laser operating up to 137 K, Appl. Phys. Lett. **83**, 5142 (2003).

[20] F. Capasso, K. Mohammed, and A. Y. Cho, Sequential resonant tunneling through a multiquantum well superlattice, Appl. Phys. Lett. **48**, 478 (1986).

[21] L. Li, L. Chen, J. Zhu, J. Freeman, P. Dean, A. Valavanis, A. G. Davies, and E. H. Linfield, Terahertz quantum cascade lasers with > 1 W output powers, Electron. Lett. **50**, 309 (2014).

[22] A. Wacker, M. Lindskog, and D. O. Winge, Nonequilibrium Green's function model for simulation of quantum cascade laser devices under operating conditions, IEEE J. Sel. Top. Quant. **19**, 1200611 (2013).

[23] D. O. Winge, M. Franckié, and A. Wacker, Simulating terahertz quantum cascade lasers: Trends from samples from different labs, J. Appl. Phys. **120**, 114302 (2016).

[24] Y. Chassagneux, Q. J. Wang, S. P. Khanna, E. Strupiechonski, J. R. Coudevylle, E. H. Linfield, A. G. Davies, F. Capasso, M. A. Belkin, and R. Colombelli, Limiting factors to the temperature performance of THz quantum cascade lasers based on the resonant-phonon depopulation scheme, IEEE Trans. Terahertz Sci. Technol. **2**, 83 (2012).

[25] A. Wacker, M. Moscoso, M. Kindelan, and L. L. Bonilla, Current-voltage characteristic and stability in resonant-tunneling n-doped semiconductor superlattices, Phys. Rev. B **55**, 2466 (1997).

[26] C. W. I. Chan, Q. Hu, and J. L. Reno, Tall-barrier terahertz quantum cascade lasers, Appl. Phys. Lett. **103**, 151117 (2013).

[27] A. Amann, K. Peters, U. Parlitz, A. Wacker, and E. Schöll, Hybrid Model for Chaotic front Dynamics: From Semiconductors to Water Tanks, Phys. Rev. Lett. **91**, 066601 (2003).

[28] T. M. Fromhold, A. Patane, S. Bujkiewicz, P. B. Wilkinson, D. Fowler, D. Sherwood, S. P. Stapleton, A. A. Krokhin, L. Eaves, M. Henini *et al.*, Chaotic electron diffusion through stochastic webs enhances current flow in superlattices, Nature (London) **428**, 726 (2004).

[29] A. E. Hramov, V. V. Makarov, A. A. Koronovskii, S. A. Kurkin, M. B. Gaifullin, N. V. Alexeeva, K. N. Alekseev, M. T. Greenaway, T. M. Fromhold, A. Patanè *et al.*, Subterahertz Chaos Generation by Coupling a Superlattice to a Linear Resonator, Phys. Rev. Lett. **112**, 116603 (2014).

[30] A. Scheuring, P. Dean, A. Valavanis, A. Stockhausen, P. Thoma, M. Salih, S. P. Khanna, S. Chowdhury, J. D. Cooper, A. Grier *et al.*, Transient analysis of THz-QCL pulses using NbN and YBCO superconducting detectors, IEEE Trans. Terahertz Sci. Technol. **3**, 172 (2013).

[31] C. Jirauschek and T. Kubis, Modeling techniques for quantum cascade lasers, Appl. Phys. Rev. **1**, 011307 (2014).

[32] M. S. Vitiello, R. C. Iotti, F. Rossi, L. Mahler, A. Tredicucci, H. E. Beere, D. A. Ritchie, Q. Hu, and G. Scamarcio, Non-equilibrium longitudinal and transverse optical phonons in terahertz quantum cascade lasers, Appl. Phys. Lett. **100**, 091101 (2012).

[33] Y. B. Shi and I. Knezevic, Nonequilibrium phonon effects in midinfrared quantum cascade lasers, J. Appl. Phys. **116**, 123105 (2014).

[34] M. Franckié, D. O. Winge, J. Wolf, V. Liverini, E. Dupont, V. Trinité, J. Faist, and A. Wacker, Impact of interface roughness distributions on the operation of quantum cascade lasers, Opt. Express **23**, 5201 (2015).

[35] A. Wacker and E. Schöll, Criteria for stability in bistable electrical devices with S- or Z-shaped current voltage characteristic, J. Appl. Phys. **78**, 7352 (1995).

[36] G. Agnew, A. Grier, T. Taimre, Y. L. Lim, M. Nikolić, A. Valavanis, J. Cooper, P. Dean, S. P. Khanna, M. Lachab *et al.*, Efficient prediction of terahertz quantum cascade laser dynamics from steady-state simulations, Appl. Phys. Lett. **106**, 161105 (2015).

[37] A. Yariv, *Quantum Electronics*, 3rd ed. (John Wiley & Sons, New York, 1988).

[38] J. J. Sakurai, *Modern Quantum Mechanics*, 1st ed. (Addison Wesley, New York, 1993).

[39] A. Wacker, Quantum cascade laser: An emerging technology, in *Nonlinear Laser Dynamics*, edited by K. Lüdge (Wiley-VCH, Berlin, 2012), Chap. 4.

[40] M. Lindskog, J. M. Wolf, V. Trinite, V. Liverini, J. Faist, G. Maisons, M. Carras, R. Aidam, R. Ostendorf, and A. Wacker, Comparative analysis of quantum cascade laser modeling based on density matrices and non-equilibrium Green's functions, Appl. Phys. Lett. **105**, 103106 (2014).